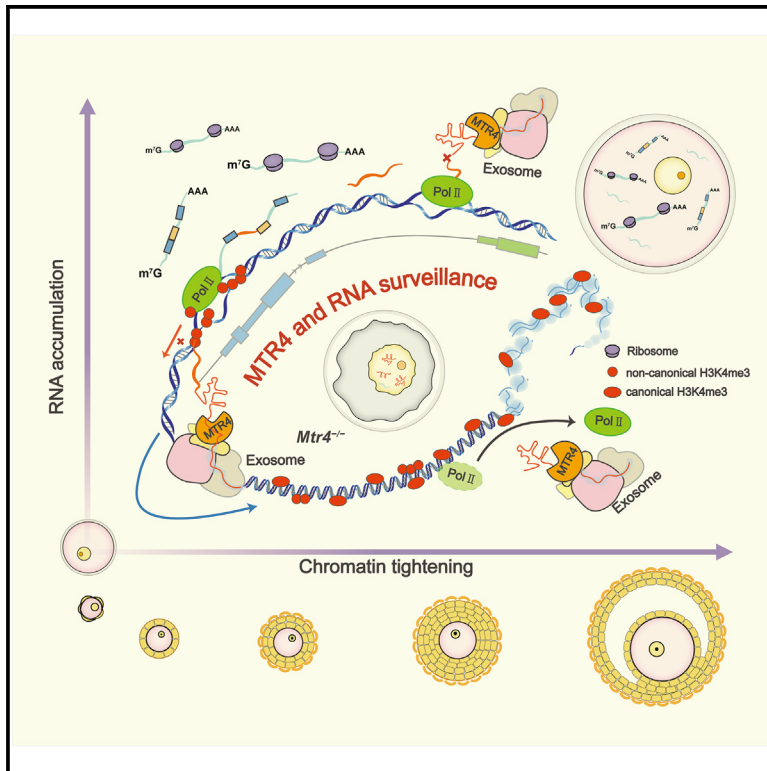# Developmental Cell

RNA surveillance by the RNA helicase MTR4 determines volume of mouse oocytes

Graphical abstract

Authors

Yun-Wen Wu, Zuo-Qi Deng, Yan Rong, ..., Xuan Wu, Hong Cheng, Heng-Yu Fan

Correspondence

hyfan@zju.edu.cn

In brief

Wu et al. demonstrated the role of MTR4-mediated RNA surveillance in oocyte maturation and volume expansion, as well as mRNA processing and storage, nuclear organization, and protein accumulation. Disrupted RNA homeostasis resulted in abnormal chromatin structure, chaotic histone modifications, and cytoplasmic immaturity.

Highlights

- RNA surveillance is responsible for the degradation of waste RNAs in the oocyte nucleus

- RNA surveillance has a feedback function in maintaining a stable nuclear environment

- MTR4 ensures the establishment of non-canonical H3K4me3 on gene bodies

- MTR4-dependent RNA surveillance is a critical checkpoint for oocyte volume growth

CellPress

Developmental Cell

 CellPress

Article

RNA surveillance by the RNA helicase MTR4 determines volume of mouse oocytes

Yun-Wen Wu,[1] Zuo-Qi Deng,[1] Yan Rong,[2] Guo-Wei Bu,[3] Yu-Ke Wu,[1] Xuan Wu,[1] Hong Cheng,[4] and Heng-Yu Fan[1,2,3,5,*]
[1]MOE Key Laboratory for Biosystems Homeostasis and Protection and Innovation Center for Cell Signaling Network, Life Sciences Institute, Zhejiang University, Hangzhou 310058, China
[2]Zhejiang Key Laboratory of Precise Protection and Promotion of Fertility, Department of Obstetrics and Gynecology, Sir Run Run Shaw Hospital, School of Medicine, Zhejiang University, Hangzhou 310016, China
[3]Center for Biomedical Research, Shaoxing Institute, Zhejiang University, Shaoxing 312000, China
[4]State Key Laboratory of Molecular Biology, CAS Center for Excellence in Molecular Cell Science, Shanghai Institute of Biochemistry and Cell Biology, Chinese Academy of Sciences, University of Chinese Academy of Sciences, Shanghai 200031, China
[5]Lead contact
*Correspondence: hyfan@zju.edu.cn
https://doi.org/10.1016/j.devcel.2024.09.009

SUMMARY

Oocytes are the largest cell type in multicellular animals. Here, we show that mRNA transporter 4 (MTR4) is indispensable for oocyte growth and functions as part of the RNA surveillance mechanism, which is responsible for nuclear waste RNA clearance. MTR4 ensures the normal post-transcriptional processing of maternal RNAs, their nuclear export to the cytoplasm, and the accumulation of properly processed transcripts. Oocytes with *Mtr4* knockout fail to accumulate sufficient and normal transcripts in the cytoplasm and cannot grow to normal sizes. MTR4-dependent RNA surveillance has a previously unrecognized function in maintaining a stable nuclear environment for the establishment of non-canonical histone H3 lysine-4 trimethylation and chromatin reorganization, which is necessary to form a nucleolus-like structure in oocytes. In conclusion, MTR4-dependent RNA surveillance activity is a checkpoint that allows oocytes to grow to a normal size, undergo nuclear and cytoplasmic maturation, and acquire developmental competence.

INTRODUCTION

Among cell types in the bodies of various species, fully grown oocytes have the largest volumes, ranging from 70 (rodents) to 2,000 (amphibians) μm in diameter. Specific mechanisms have been employed to support significant oocyte growth. In insects, nurse cells transfer material to oocytes through cytoplasmic bridges connecting the two cell types.[1] In fishes and amphibians, yolk proteins synthesized in the liver are transported to oocytes via blood circulation.[2] As an extreme example, gene clusters encoding ribosomal RNAs (rRNAs) have been amplified in fast-growing *Xenopus* oocytes to facilitate rRNA synthesis.[3] However, similar mechanisms do not exist during mammalian oogenesis. Studies have shown that the dormancy and awakening of primordial follicles is mainly determined by the activity of the phosphatidylinositol 3-kinase mechanistic target of rapamycin protein kinase B [(PI3K)-mTOR-AKT] signaling pathway.[4,5] The genes and pathways supporting mammalian oocyte growth after primordial follicle awakening remain poorly understood.

Oocyte growth is accompanied by a significant accumulation of RNAs transcribed from the oocyte genome. These maternal RNAs and proteins are stored in the germinal vesicle (GV) and ooplasm to support meiotic maturation and early zygotic development.[6,7] RNA precursors can be misfolded, fail to assemble into larger complexes, or may be incorrectly processed. The resulting mutation-containing mRNAs encode truncated and toxic proteins.[8] Cells also contain junk RNAs derived from the bidirectional transcription of the promoters of protein-coding genes. These misprocessed RNAs must be distinguished and degraded from normal RNAs that should be retained because failure to remove these RNAs can alter the transcription of adjacent protein-coding genes, resulting in DNA damage and chromosomal rearrangements.[9] The intracellular quality control pathways that target defective RNAs for degradation are referred to as RNA surveillance.[10] Despite studies in cultured human cell lines and model systems such as worms and fruit flies,[11–13] the potential roles of RNA processing and surveillance in extraordinary mammalian oocyte growth and the associations of RNA surveillance with reproductive and developmental defects have not been sufficiently investigated.

The major effectors of the RNA surveillance pathways are ribonucleases, which degrade defective RNAs. Most ribonucleases function as multiunit complexes, relying on protein cofactors or adaptors that recognize defective RNAs and recruit nucleases. Among these protein complexes, RNA exosome catalyzes 3′-to-5′ processing or degradation of a vast array of different RNA substrates and contributes to translation-dependent mRNA surveillance pathways, such as nonstop decay, nonsense-mediated decay, and no-go decay.[14–16] The RNA

exosome includes a barrel-shaped nine-subunit core that interacts with the nuclease DIS3 (in the nucleus) or DIS3-like (DIS3L in the cytoplasm) to form a 10-subunit complex.[17–19] In all studied eukaryotic species, RNA helicase mRNA transporter 4 (MTR4) is a crucial adaptor subunit of exosomes.[20–22] Helicase activity allows MTR4 to unwind high-dimensional RNA structures and deliver single-stranded RNAs threaded down through the central channel of the exosome for degradation.[20,23,24] Through interactions with nuclear poly(A)-binding protein 1 (PABPN1), MTR4 targets polyadenylated RNA polymerase II (RNA Pol II) transcripts that are prematurely terminated or generated by bidirectional promoter activity for degradation.[25] Recent gene knockout studies have demonstrated that PABPN1 and the exosome subunit exosome component (EXOSC10 [also known as RRP6]) are required to maintain RNA homeostasis and sculpt the transcriptome in growing mouse oocytes and preimplantation embryos.[26–28] However, the role of MTR4, which is involved in a wider spectrum of exosomal functions than those of PABPN1 or EXOSC10, remains unclear.

In this study, we profiled nuclear and cytoplasmic RNA processing characteristics during oocyte growth using RNA sequencing (RNA-seq) approaches and elucidated the function of MTR4 in regulating mRNA homeostasis during oogenesis, particularly its feedback impact on transcription, histone modifications, and chromatin configurations. These results indicated that MTR4-dependent RNA surveillance activity is a critical checkpoint that allows mammalian oocytes to grow to an extraordinary size.

RESULTS

Proper mRNA accumulation in the cytoplasm is essential for oocyte growth

The oocyte is the biggest cell type in mammals. The volume of mouse oocytes increases nearly 500 times during the long growth period (Figure 1A). However, the question remains as to why oocytes can grow in large volumes. Through *in situ* measurements of ovarian sections, we quantified that during the growth process, the diameter of the cytoplasm expanded drastically, especially around the secondary follicle period (Figure 1B). In contrast, the growth rate of the nucleus showed a gentle trend (Figure 1B). Correspondingly, the nucleus-cytoplasm volume ratio of oocytes constantly decreased after being activated at the primordial follicle stage, dropping from 12.6% at the primary follicle stage to 3.8% at the antral stage (Figure 1C). However, the constant decrease in the nucleus-cytoplasm volume ratio is a rather special pattern, as somatic cells tend to maintain a stable nucleus-cytoplasm volume ratio of approximately 8%, according to published results (Figure 1C).[29] We conducted poly(A) RNA sequencing using samples derived from different developmental stages, with the External RNA Control Consortium (ERCC) spike-in for normalization. Because the first wave of follicle development is relatively synchronous and well characterized in mice, we collected transcriptome sequencing data of oocytes from representative stages of ovaries on day 5 (awakened oocytes start to grow at the primary follicle stage), day 14 (growing oocytes at the secondary follicle stage), day 21 (oocytes at the end of growth and undergoing non-surrounded nucleolus-surrounded nucleolus [NSN-SN]

transition in antral follicles), and day 56 (fully grown oocytes arrested at the GV stage awaiting ovulation and having accomplished the NSN-to-SN transition). Using ERCC spike-in calibration, we found that the overall mRNA level in oocytes rose nearly 8-fold from days 5 to 21 and remained constant thereafter (Figure 1D).

To investigate the pattern of subcellular RNA accumulation during oocyte growth, we separated the nuclei and cytoplasm of oocytes using micromanipulation and constructed a poly(A) RNA sequencing library (Figures 1E and S1A). GV (nuclei) and ooplasms were collected from mice on post-natal days 14, 21, and 56. The general transcription activity of oocytes at each stage was verified by a 5′-ethynyl uridine (EU) incorporation assay (Figures S1B and S1C). To verify the efficiency of nucleus-cytoplasm separation, we examined the expression patterns of mitochondria-related genes. All of them were highly expressed in the ooplasm but barely detected in the nuclei (Figure S1D). Using ERCC spike-in calibration, we found that the overall mRNA level in the ooplasm significantly increased from days 14 to 21 and remained at a comparable level from days 21 to 56. In contrast, the mRNA levels in the nuclei continued to decrease from days 14 to 56 (Figure 1F). Changes in the mRNA levels of different subcellular components during oocyte growth revealed that most mRNAs were transported and stored in the ooplasm after being transcribed in the nucleus, and the cytoplasm-nucleus mRNA content ratio continued to increase until finally reaching nearly 59-fold at the fully grown GV stage (Figure 1F).

We analyzed the characteristic differences between cytoplasmic and nuclear transcripts. Intron splicing is essential for pre-mRNA processing, and the alternative splicing of introns contributes to transcriptional plasticity of the transcriptome.[30,31] Thus, we conducted intron retention (IR) analyses among different groups using the IRFinder software.[32] Based on the intron retention events detected by IRFinder, we conducted intron quantifications among different sequencing groups. Distribution maps of retained introns for individual biological replicates are shown in Figure S1E.

In poly(A) RNA-seq, mature post-transcriptional RNAs with long poly(A) tails are preferentially reverse-transcribed during sequence library construction. In contrast, immature or non-coding RNAs without polyadenylation have not been documented in poly(A) RNA-seq. Thus, we conducted total RNA-seq, which revealed comprehensive co-transcriptional information (Figure 1G). Nuclei and ooplasms separated from day-21 oocytes were used for total RNA-seq. More retained introns were identified in the nuclei using total RNA-seq than poly(A) RNA-seq (Figure 1G). When we compared the retained introns detected in the two sequencing methods, introns specifically detected in total RNA-seq were defined as co-transcriptionally spliced introns. In contrast, the retained introns detected using poly(A) RNA-seq on day-21 nuclei were post-transcriptionally retained introns because they were retained after polyadenylation. Co-transcriptionally spliced introns were preferentially located in the first quarter and the middle of the gene body, whereas post-transcriptionally retained introns detected using poly(A) RNA-seq were concentrated in the first quarter of the gene body (Figure 1H).

Furthermore, poly(A) RNA-seq also detected more IR events in the nuclei of day-14 oocytes than in day-21 oocytes, whereas no
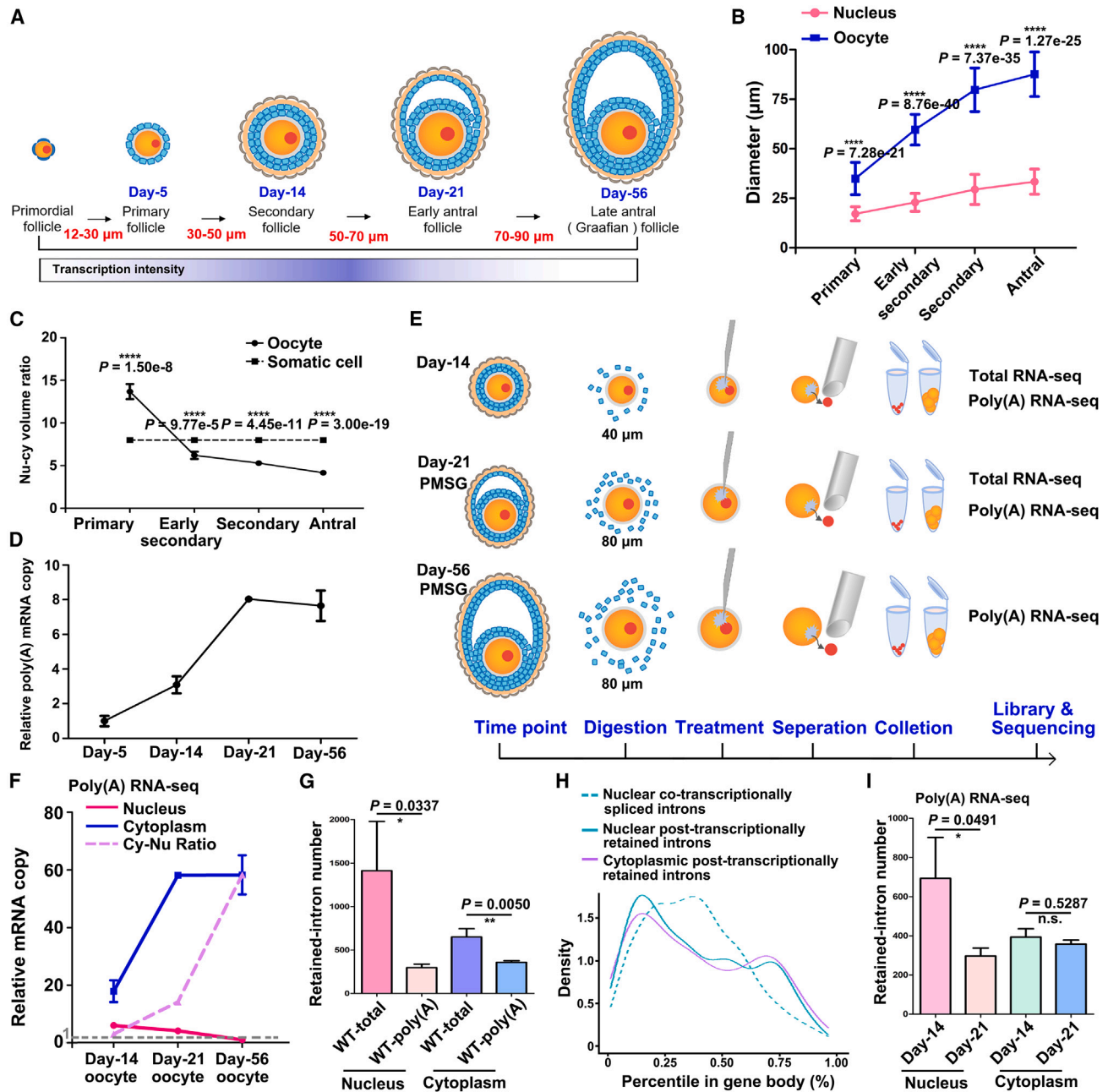
CellPress

Figure 1. Proper mRNA accumulation in ooplasm is essential for oocyte growth

(A) A diagram showing changes during mouse follicle growth. The color bar on the bottom indicates transcription activity changes.

(B) Quantitative measurements of nucleus and oocytes' diameter in follicles from different developmental stages. $n \geq 25$ per group.

(C) Nucleus-cytoplasm volume ratio calculated from (B).

(D) Relative mRNA levels in oocytes derived from mice of different ages.

(E) Workflow of nucleus-cytoplasm separation for RNA sequencing (RNA-seq).

(F) Relative mRNA levels in the nucleus and ooplasm from day-14, -21, and -56 oocytes.

(G) Numbers of retained introns detected in different RNA-seq groups.

(H) Density map showing the distribution of retained introns in the gene body.

(I) Numbers of retained introns detected in different RNA-seq groups.

Data are represented as mean ± SEM.

See also Figure S1.

CellPress

Developmental Cell
Article

obvious differences were found in the cytoplasm (Figure 1I). The decrease in IR events in the nuclei from days 14 to 21 detected using poly(A) RNA-seq indicated post-transcriptionally splicing events of polyadenylated RNAs during oocyte growth. When comparing co-transcriptionally spliced introns detected in day-21 nuclei using total RNA-seq, post-transcriptionally spliced introns detected in day-14 nuclei using poly(A) RNA-seq, and retained introns in day-21 nuclei using poly(A) RNA-seq, introns located in the middle part of the gene body are preferentially spliced during RNA processing, whereas introns in the 5′ and 3′ quarters are selectively retained (Figure S1F). However, in the ooplasm, no obvious differences in the retained introns were found between days 14 and 21 in the poly(A) RNA-seq (Figure S1G).

Bioinformatics analyses revealed distinct differences in content as well as characteristics of transcripts between different subcellular groups, namely that many mRNAs were transcribed and processed in the nucleus and then transported to the ooplasm for storage during oocyte growth. Temporarily retained RNAs in the nucleus during oocyte growth were removed during nuclear maturation. The complexity and length of this process implies a potential surveillance mechanism for mRNA regulation during oogenesis.

Exosome-associated RNA helicase mtr4 is crucial for oocyte growth

Exosomes are evolutionarily conserved nuclear RNA degradation complexes (Figure S2A). The constituents of the exosomes were highly expressed in growing oocytes (Figure S2B). MTR4 is the only known exosome-associated RNA helicase that unwinds RNAs for degradation. MTR4 was expressed in mouse oocytes during the growth stage and was downregulated at the metaphase II stage (Figure 2A). Endogenous MTR4 localized in the oocyte nucleus (Figures 2B and S2C). Furthermore, mCherry-MTR4 expressed using mRNA microinjection showed nuclear localization with a higher concentration around the nucleolus-like body in GV oocytes (Figure S2D). GFP-tagged DDB1-CUL4-associated factor 13 (DCAF13, a nucleolar protein) was co-expressed to visualize the nucleolus (Figure S2D). We generated oocyte-specific *Mtr4*-knockout mice using *Zp3-Cre* (Figure S2E) and confirmed the knockout efficiency (Figures 2B and 2C).

Mtr4^fl/fl^;Zp3-Cre female mice were completely infertile (Figure S2F). Growing oocytes from day-14 *Mtr4^fl/fl^;Zp3-Cre* mice had normal size and morphology. When control oocytes underwent remarkable increases in size from days 14 to 21, the growth of oocytes in *Mtr4^fl/fl^;Zp3-Cre* mice over the same period was impaired (Figures 2D and 2E). In addition to their sizes being smaller than wild-type (WT) oocytes, *Mtr4*-deleted oocytes exhibited other abnormalities, including thinner zonal pellucida, enlarged perivitelline space, and increased granularity in the ooplasm (Figure 2D). During *in vitro* maturation, oocytes isolated from day-21 *Mtr4^fl/fl^;Zp3-Cre* mice failed to undergo GV breakdown (Figure 2F). No metaphase II eggs were obtained after the superovulation treatment (Figure 2G).

Mtr4 deletion leads to disorders of RNA homeostasis in oocytes

Poly(A) RNA-seq was performed using oocytes isolated from *Mtr4^fl/fl^* and *Mtr4^fl/fl^;Zp3-Cre* mice on days 14 and 21. The gene

expression level was assessed as fragments per kilobase of transcript per million mapped reads (FPKM) and corrected using ERCC spike-in (Table S1; Figures S3A and S3B). Although the oocytes of day-14 *Mtr4*-null oocytes were morphologically normal, 833 and 136 transcripts were upregulated and downregulated, respectively (Figure 2H). Differences in transcript levels were more apparent in day-21 *Mtr4*-null oocytes, in which 2,446 and 2,898 transcripts were upregulated and downregulated, respectively (Figure 2I). These upregulated or downregulated transcripts on day 21 included most upregulated or downregulated transcripts in day-14 *Mtr4*-null oocytes (Figures S3C and S3D), indicating that the effect caused by *Mtr4* knockout accumulated during oocyte growth. Moreover, most of the upregulated transcripts in day-21 *Mtr4*-null oocytes were degraded in WT oocytes from days 14 to 21, whereas most downregulated transcripts in *Mtr4*-null oocytes on day 21 accumulated in WT oocytes from days 14 to 21 (Figures 2J and 2K), suggesting that normal mRNA turnover during oocyte growth was disrupted by *Mtr4* deletion. However, no significant differences in global mRNA levels were observed between *Mtr4*-null and *Mtr4^fl/fl^* oocytes (Figure 3L). Differentially expressed genes (DEGs) were involved in various functions during oocyte growth and maturation, including DNA damage repair, chromatin remodeling, epigenetic regulation, etc. (Figures S3E and S3F).

To investigate whether the DEGs in oocytes after *Mtr4* deletion were caused by inhibition of the exosome-mediated RNA degradation pathway, we compared DEGs in *Mtr4*-null oocytes from our study with DEGs in *Exosc10*-null oocytes and *Pabpn1*-null oocytes from published data.[26,33] Pairwise scatterplots generated from fold changes of expression levels in *Mtr4*-null oocytes and *Exosc10*-null oocytes or *Pabpn1*-null oocytes showed that most of the shared DEGs had the same trend between the two genotypes (Figures S3G and S3H). Compared with the *Pabpn1*-null and *Exosc10*-null oocytes, the *Mtr4*-null oocytes had more DEGs, indicating that the *in vivo* functions of MTR4 were related but did not totally overlap with those of EXOSC10 and PABPN1 (Figures 2M and 2N).

Mtr4 deletion results in the accumulation of RNAs in the nucleus and blockage of cytoplasmic mRNA storage

We further investigated whether the transcriptome disorders caused by *Mtr4* deletion had subcellular characteristics. We performed fluorescence *in situ* hybridization (FISH) using RNA probes targeting poly(A) (50 nt) RNAs. The results indicated that large amounts of RNAs with poly(A) tails accumulated in the nuclei of *Mtr4*-null oocytes (Figures 3A and 3B).

Next, we conducted a nucleus-cytoplasm separation experiment in oocytes from day-21 mice, followed by poly(A) RNA-seq and total RNA-seq (Figures S4A–S4D). The mRNA content rose three times in the nucleus and decreased by 50% in the cytoplasm after *Mtr4* deletion (Figure 3C). Using poly(A) RNA-seq, we detected 4,601 upregulated transcripts in the nucleus and 5,141 downregulated transcripts in the cytoplasm of *Mtr4*-null oocytes (Figures 3D and 3E; Table S2). Transcripts encoding important maternal factors, such as *Gdf9*, *Bmp15*, and *Cxxc1*,[34,35] decreased in the cytoplasm of *Mtr4*-null oocytes (Figures 3D and 3E), but these changes were not observed in poly(A) mRNA-seq using whole oocytes (Figures 2H and 2I). A similar trend was observed in total
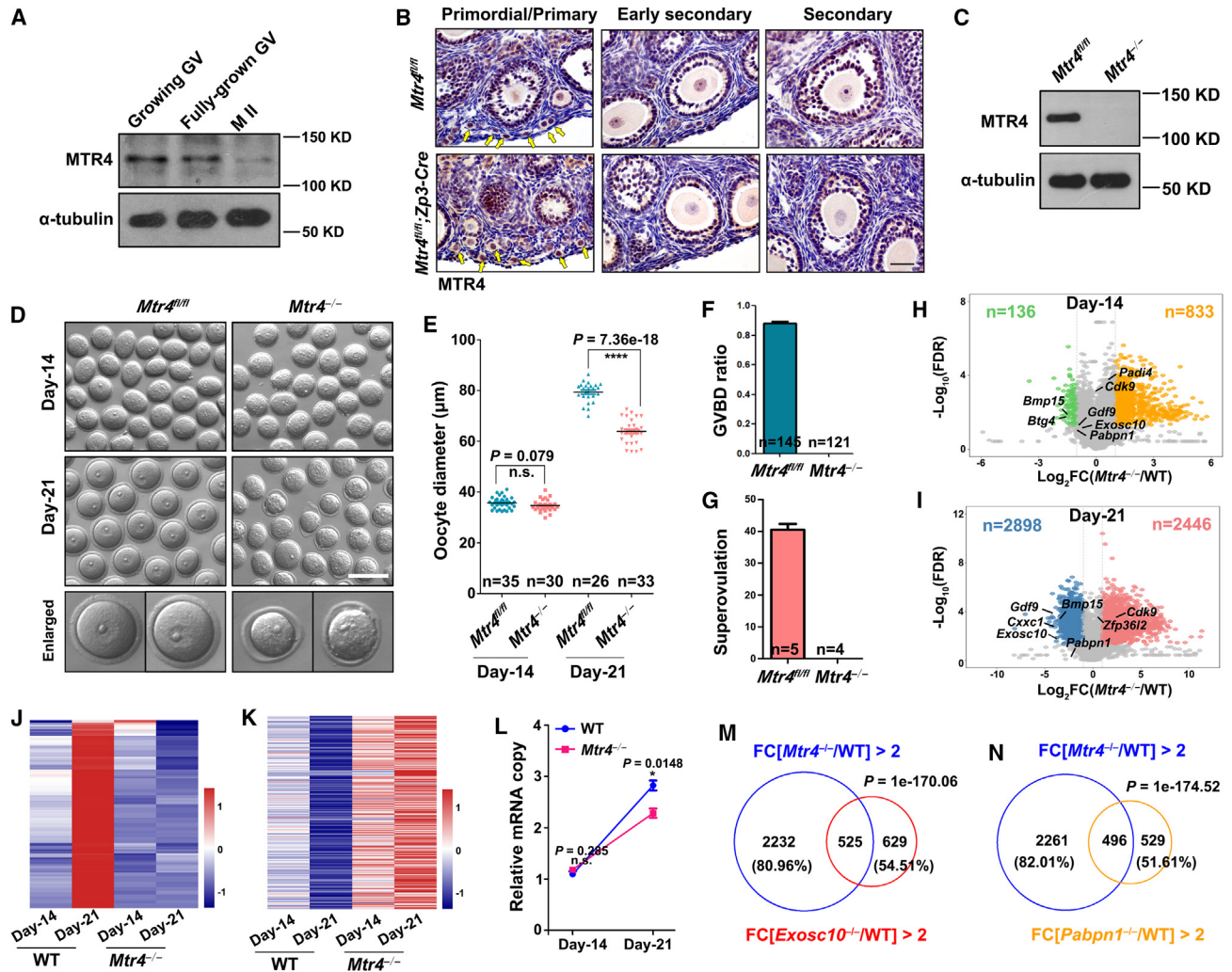
Figure 2. MTR4 is required for oocyte maturation and RNA homeostasis

(A) Western blot results showing MTR4 levels in mouse oocytes. Total proteins from 250 oocytes were loaded in each lane. α-tubulin served as a loading control.

(B and C) Immunohistochemistry (B) and western blot (C) results showing MTR4 expression in oocytes. Arrows indicate oocytes in primordial follicles.

(D) Representative images of oocytes collected from $Mtr4^{fl/fl}$ and $Mtr4^{fl/fl};Zp3$-Cre mice.

(E) Diameters of oocytes in (D). $n \geq 26$ per group.

(F) GVBD ratio of oocytes derived from day-23 mice primed with PMSG for 48 h. $n \geq 121$ per genotype.

(G) Numbers of oocytes collected from oviducts of day-24 mice after superovulation. $n \geq 4$ per genotype.

(H and I) Scatterplot of the relative levels of transcripts in the $Mtr4^{fl/fl}$ and $Mtr4$-null oocytes. Differentially expressed transcripts are highlighted. FC, fold change.

(J and K) Heatmap showing relative expression levels of genes downregulated (J) and upregulated (K) during oocyte growth after $Mtr4$ deletion.

(L) Changes of relative mRNA copy numbers in $Mtr4^{fl/fl}$ and $Mtr4$-null oocytes normalized by ERCC spike-in.

(M and N) Venn diagram shows the overlap of accumulated transcripts in day-21 $Mtr4$-null and $Exosc10$-null oocytes (M) or day-21 $Mtr4$-null and $Pabpn1$-null oocytes (N).

Scale bars: 50 μm in (B) and (C), 100 μm in (D). Data are represented as mean ± SEM.

See also Figures S2 and S3 and Table S1.

RNA-seq data that more nuclear transcripts accumulated whereas more cytoplasmic RNAs were downregulated in day-21 *Mtr4-null* oocytes (Figures 3F and 3G; Table S3). Transcriptome changes in day-14 oocytes were also analyzed using total RNA-seq, which was consistent with that of day 21 (Figures S4E–S4H; Table S3). The disorder of subcellular mRNA distribution implied that *Mtr4* deletion led to large-scale accumulation of nuclear mRNAs and the blockage of cytoplasmic mRNA storage.

Based on the globally chaotic subcellular distribution of RNA revealed using poly(A) RNA-seq and total RNA-seq, RT-qPCR was performed to verify this hypothesis. Results of RT-qPCR showed a consistent upregulation in the nucleus-to-cytoplasm ratio of *Gdf9*, *Btg4*, and *Zp2* between WT and *Mtr4*-null oocytes (Figure 3H). FISH probes targeting the exons of transcripts encoding important oocyte-specific factors, including *Gdf9* and *Btg4*, were used to further support the conclusion. Both *Gdf9*-exon and *Btg4*-exon signals were upregulated in the nuclei of
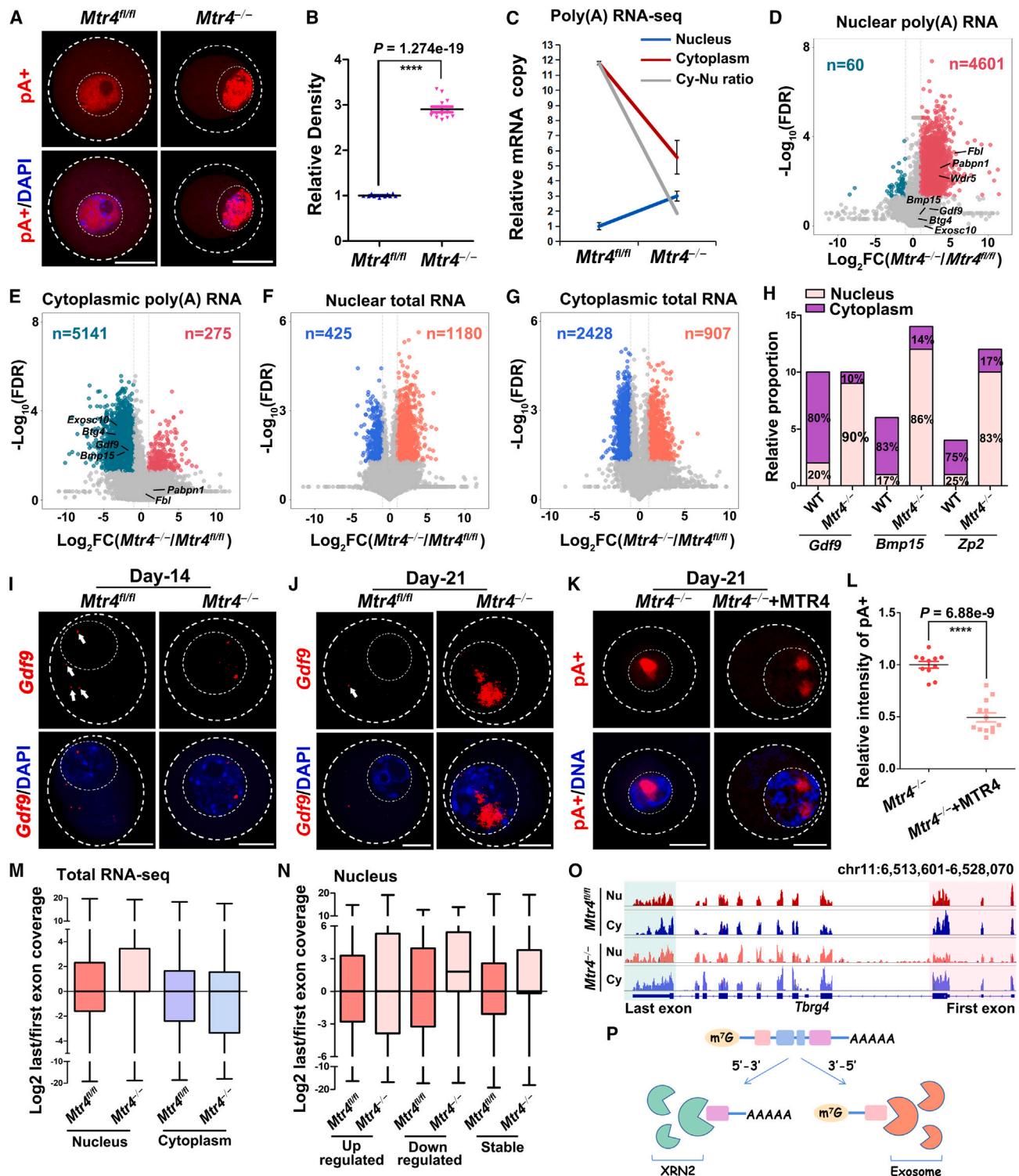
Figure 3. *Mtr4* deletion results in the accumulation of RNAs in the nucleus

(A and B) Fluorescence *in situ* hybridization (FISH) of poly(A) RNAs in oocytes. $n \geq 13$ per genotype.

(C) Relative mRNA copy numbers in oocytes detected by poly(A) RNA-seq, normalized by ERCC.

(D and E) Scatterplot of the relative levels of transcripts in the nucleus and ooplasm of the *Mtr4^fl/fl^* and *Mtr4*-null oocytes in poly(A) RNA-seq. FC, fold change.

(F and G) Scatterplot of the relative levels of transcripts in the nucleus and ooplasm of the *Mtr4^fl/fl^* and *Mtr4*-null oocytes in total RNA-seq. FC, fold change.

(H) RT-qPCR results showing relative expression levels of several growing factors in the nucleus and cytoplasm extracted from oocytes.

(I and J) FISH probes recognizing the exons of *Gdf9* in oocytes. White arrows indicate *Gdf9* exon signals in the cytoplasm. $n \geq 12$ per genotype.

(legend continued on next page)

Developmental Cell
Article

Mtr4-deleted oocytes and reduced in the cytoplasm, and the trend was strengthened from days 14 to 21 (Figures 3I, 3J, and S4I), which was similar to the tendency shown in poly(A) FISH experiments (Figures 3A and 3B). We replenishing MTR4 in day-21 *Mtr4*-null oocytes by microinjection of *Gfp-Mtr4* mRNA (Figures S4J and S4K) and further conducted a poly(A) FISH experiment on both non-injected and microinjected *Mtr4*-null oocytes. The results showed that poly(A) signals in the nuclei of microinjected *Mtr4*-null oocytes decreased by ∼50% with the exogenous expression of MTR4 (Figures 3K and 3 L), supporting the conclusion that absence of MTR4 causes nuclear retention of mRNAs in oocytes.

Normal transcription with integrity was supposed to have balanced read coverage across the gene body, whereas abnormal RNA degradation events, as well as interrupted transcription, may lead to RNAs without integrity. By comparing the read coverage between the first and last exons in sequencing data, RNA integrity can be revealed. Total RNA-seq data were used instead of poly(A) RNA-seq to avoid 3′ end bias. By comparing the coverage between the first and last exons in the total RNA-seq data, we found significantly increased read coverage in the last exon compared with the first exon only in the *Mtr4*-null nucleus (Figure 3M), indicating that nuclear-retained transcripts in *Mtr4*-null oocytes contained RNAs with 5′ end absence. When further comparing the last/first exon coverage ratio in DEGs and stable transcripts retained in the nucleus of *Mtr4*-null oocytes, the downregulated transcripts varied the most and the stable group also showed a biased tendency (Figure 3N), whereas transcripts with different expression levels in cytoplasm did not show an obvious bias of exon coverage (Figure S4L). Integrated Genomics Viewer (IGV) snapshots present an example of imbalanced exon distribution in *Mtr4-null* nucleus (Figure 3O). By designing primers targeting the first or last exon, respectively, biased read coverage between the first and last exons was also verified by RT-qPCR, with several examples (Figure S4M). Because transcripts with 5′ end absence were unlikely to have resulted from interrupted transcriptions, we speculated that *Mtr4* knockout disrupted the nuclear RNA 3′-5′ degradation pathway, but the nuclear RNA 5′-3′ degradation pathway remained intact, therefore causing higher degradation rates of 5′ end exons than 3′ end exons (Figure 3P).

Dysfunction of nuclear RNA surveillance results in the nucleus-to-cytoplasm transport of transcripts without proper processing

To further validate the molecular characteristics of the retained transcripts in *Mtr4*-null oocytes, IR events were examined in total RNA-seq data using IRFinder software with the criteria described previously. More abundant IR events were detected in both the nucleus and cytoplasm of *Mtr4*-null oocytes compared with that in *Mtr4^{fl/fl}* oocytes, suggesting that MTR4 is essential for removal of co-transcriptionally spliced introns (Figure 4A). When total RNA-seq reads were annotated to the genome, the proportion of exons decreased in the nucleus and cytoplasm of *Mtr4*-null oocytes, whereas the proportions of introns and intergenic regions increased nearly 2-fold (Figure 4B). When normalizing intron reads with FPKM, read numbers of 3,087 and 2,671 introns were upregulated in *Mtr4*-null nuclei and cytoplasm, respectively (Figures 4C and 4D). To compare the levels of retained introns in upregulated nuclear RNAs after *Mtr4* deletion (Figure 3D), we generated heatmaps with intron FPKM across different subcellular group, and FPKM reads were normalized with *Z* score method. 71.2% of the transcripts (clusters I and II) had more nuclear IR after *Mtr4* deletion, and 34.4% were further transported to the cytoplasm (cluster II) (Figure 4E). IGV snapshots showed two examples in which the transcripts containing retained introns were stabilized in the nucleus, and some of them were further exported to the cytoplasm (Figures 4F and 4G).

FISH experiments showed that *Gdf9*-intron signals were detected in both the nucleus and cytoplasm of *Mtr4*-null oocytes, whereas in WT oocytes, only a few signals were detected in the nucleus (Figure 4H). We further confirmed IR events using RT-qPCR (Figure 4I). F-R1 primers examined the expression levels of transcripts, with or without retained introns, whereas the F-R2 primers specifically examined transcripts with retained introns. The IR ratio was calculated as the number of transcripts with retained introns divided by the total number of transcripts. *Gdf9* and *Noxo1* were almost undetectable in WT nuclei; however, a large proportion of *Gdf9* with retained introns was detected in the nuclei of *Mtr4*-null oocytes (Figures 4J and 4K). Moreover, a higher proportion of intron-retained *Gdf9* and *Noxo1* was detected in the cytoplasm of *Mtr4*-null oocytes than in WT oocytes (Figures 4J and 4K). When replenishing MTR4 in day-21 *Mtr4*-null oocytes by microinjection of *Mtr4* mRNA, the IR ratio of *Gdf9*, *Noxo1*, and *Zp2* in *Mtr4*-null oocytes decreased by 50% (Figure 4L).

RNA processing has been reported to occur in the nuclear speckles. Nuclear poly(A) binding protein PABPN1 and serine- and arginine-rich splicing factor 2 (SRSF2) localize in nuclear speckles.[26,36] Immunofluorescence results showed that in growing oocytes from day-14 WT mice, nuclear speckles were plenty but small (Figures S5A–S5C). However, SRSF2 and PABPN1 were evenly distributed in *Mtr4*-null oocytes, with fewer foci (Figures S5A–S5C). On day 21, fewer but larger foci were formed in *Mtr4^{fl/fl}* oocytes, whereas no foci were found in day-21 *Mtr4*-null oocytes (Figures S5A–S5C). When replenishing MTR4 in day-21 *Mtr4*-null oocytes by microinjection of *Mtr4* mRNA, 36.4% of the oocytes were able to re-form larger nuclear speckles and more small foci were formed in the left 63.6%

(K) FISH probes recognizing the poly(A) in *Mtr4*-null oocytes and *Mtr4*-null oocytes with exogenously expressed MTR4. *n* ≥ 11 per genotype.
(L) Quantification of poly(A) fluorescent signals in (K).
(M) Boxplot showing the coverage ratio of last exon/first exon in nuclear and cytoplasmic total RNA-seq data in oocytes.
(N) Boxplot showing the coverage ratio of last exon/first exon of different expressed or stable genes in nuclear total RNA-seq data.
(O) IGV snapshots showing representative examples in (M).
(P) An overview illustrating two main degradation pathways in the nucleus.
Scale bars: 30 μm in (A) and (K), 25 μm in (I) and (J). Data are represented as mean ± SEM.
See also Figure S4 and Tables S2 and S3.

(legend on next page)

Developmental Cell
Article

CellPress
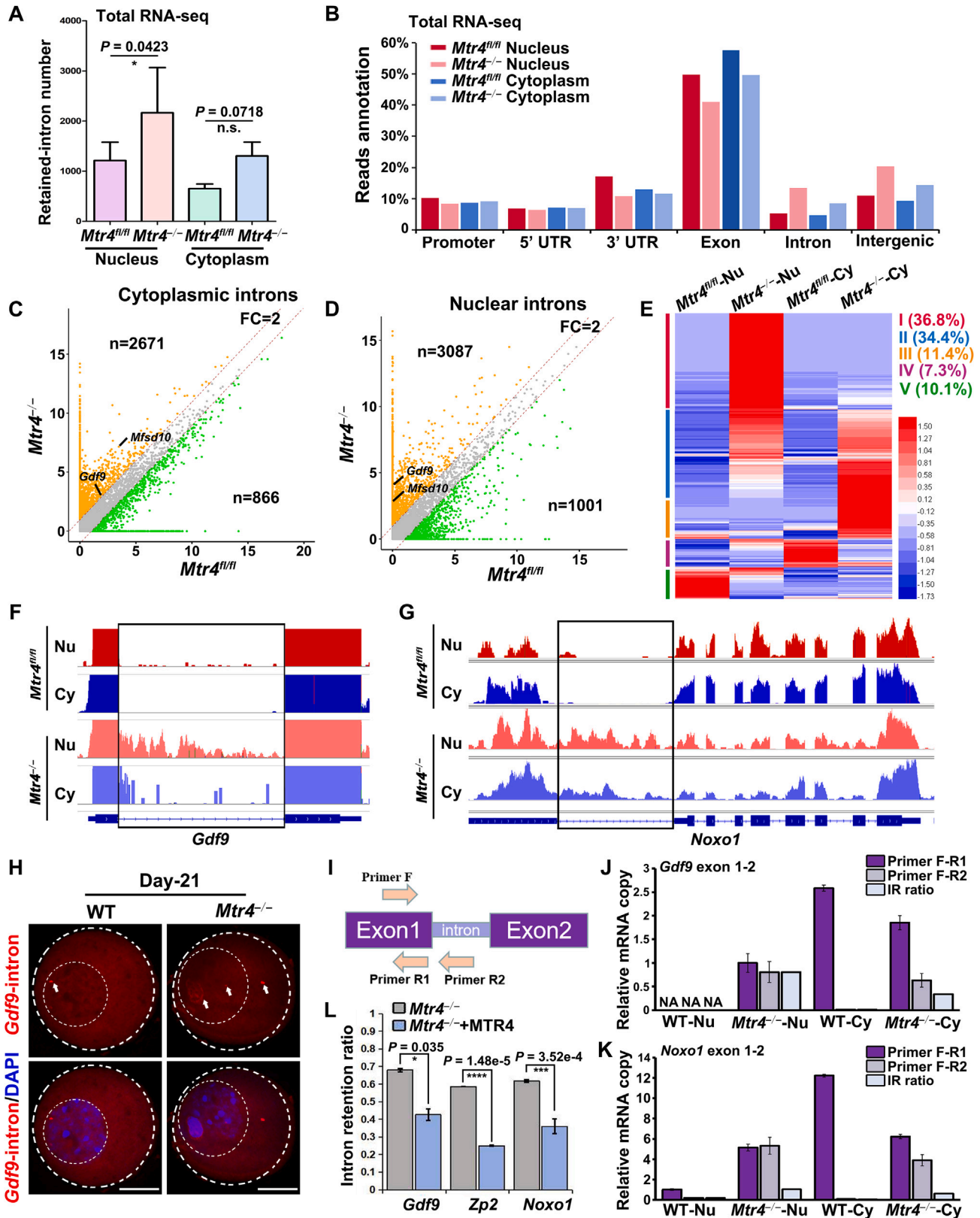
oocytes, confirming that the formation of nuclear speckles partly depends on the presence of MTR4 (Figure S5A). The absence of nuclear speckles partly explains the RNA processing dysfunction in *Mtr4*-null oocytes.

Dysfunction of RNA surveillance leads to the failure of chromatin to configure transition during oocyte growth

Growing oocytes derived from day-14 *Mtr4^{fl/fl};Zp3-Cre* mice had an NSN chromatin configuration, whereas all oocytes derived from day-21 *Mtr4^{fl/fl};Zp3-Cre* mice failed to accomplish the NSN-to-SN transition, and no nucleolus-like structures were formed in day-21 *Mtr4*-null oocytes (Figure 5A). As the chromatin configuration shifts from the NSN to the SN, oocytes undergo transcriptional silencing. RNA synthesis activity was high in day-14 oocytes but absent in day-21 fully grown WT oocytes following the NSN-to-SN transition (Figure 5B). However, in *Mtr4*-null oocytes, the EU incorporation signal was still present on day 21 when transcription was silenced in WT oocytes (Figure 5B). Co-immunofluorescence of phosphorylated RNA Pol II at serine-2, another marker of active transcription, showed a pattern similar to that of EU staining (Figure S6A).

We conducted an assay for transposase-accessible chromatin using high-throughput sequencing (ATAC-seq) of oocytes derived from day-21 mice (Figure S6B). A total of 172,111 peaks were detected in *Mtr4*-null oocytes, nearly 3-fold higher than the 59,445 peaks in *Mtr4^{fl/fl}* oocytes. Moreover, 59.6% of the peaks (35,455) in *Mtr4^{fl/fl}* oocytes overlapped with those in *Mtr4*-null oocytes (Figure 5C). Peak profiling and heatmaps indicated higher chromatin accessibility at the transcription start sites (TSSs) and around the transcription ending sites in *Mtr4*-null oocytes (Figure 5D). Snapshots showed that the genome of *Mtr4*-null oocytes had a more abundant and higher enrichment pattern than that of *Mtr4^{fl/fl}* oocytes, indicating defects in chromatin condensation (Figure 5E). *Mtr4*-null oocytes showed a higher proportion of promoter peaks, which corresponded to higher chromatin accessibility at the TSSs, suggesting that the failure of chromatin condensation in these oocytes may contribute to consistent transcription (Figure 5F). Pairwise scatterplots were generated using the fold changes of FPKM from poly(A) RNA-seq and the fold changes of Reads Per Kilobase per Million mapped reads (RPKM) from ATAC-seq between *Mtr4^{fl/fl}* and *Mtr4*-null oocytes. Scatterplots showed a similar trend of change between RNA-seq and ATAC-seq, where the increased chromatin accessibility associated with upregulation of transcript expression levels (Figure 5G). Chromatin regions around transcription ending sites usually had higher accessibility in upregulated genes than in downregulated genes in *Mtr4*-null oocytes

(Figure 5H). *Mtr4* deletion resulted in 6,744 genes with an open promoter; however, only 2,024 transcripts (30.0%) belonged to genes that accumulated during oocyte growth in RNA-seq, suggesting that the abnormally open chromatin of *Mtr4*-null oocytes resulted in the ectopic expression of non-maternal genes (Figure 5I). Genes with higher levels of chromatin accessibility in promoters after *Mtr4* deletion usually had higher expression levels than those with downregulated open promoters, indicating that an increase in chromatin accessibility is associated with transcriptional activation in oocytes and may prevent genome silencing at this stage (Figure 5J).

MTR4 is required for the transition of genomic H3K4me3 distribution from canonical to non-canonical type during oogenesis

An abnormal nuclear environment has been shown to affect chromatin structural transition and transcription.[37–40] Therefore, we assessed whether H3K4me3, an important transcription-related histone modification, is established after *Mtr4* deletion. Immunofluorescence results showed that H3K4me3 signals increased from days 14 to 21 in control oocytes but not in *Mtr4*-null oocytes (Figure 6A). We conducted H3K4me3 cleavage under targets and mentation (CUT&Tag) experiment using day-21 oocytes (Figure S6C). More CUT&Tag peaks (3-fold) were detected in *Mtr4^{fl/fl}* oocytes. These peaks included 86.6% of those detected in *Mtr4*-null oocytes (Figure 6B). Whole-genome annotation of CUT&Tag peaks showed that 56.2% of the H3K4me3 peaks were located in the promoters of *Mtr4*-null oocytes. In contrast, only 27.2% were detected in the promoters of *Mtr4^{fl/fl}* oocytes (Figure 6C). In contrast, the proportion of H3K4me3 peaks decreased in the gene body and intergenic region after *Mtr4*-ablation (Figure 6C). Although the number of genes with H3K4me3 signals in the promoters was comparable between the two groups (Figure 6D), the number of genes with H3K4me3 signals in the gene bodies decreased in *Mtr4*-null oocytes (Figure 6E).

H3K4me3 signals were more enriched near the TSSs in *Mtr4*-null oocytes than in control oocytes due to the lack of H3K4me3 distribution in non-promoter regions (Figure 6F). The deposition of non-canonical broad H3K4me3 peaks at distal gene loci during oocyte maturation normally coincides with genome silencing.[35,41,42] *Mtr4^{fl/fl}* oocytes tended to obtain a non-canonical form of broad H3K4me3 distribution (marked in yellow), whereas *Mtr4*-null oocytes had typical canonical H3K4me3 peaks (marked in purple), similar to the H3K4me3 distribution in WT day-14 oocytes from published data,[33] indicating that *Mtr4* knockout impaired the establishment of broad H3K4me3 peaks during oocyte maturation (Figure 6G).

Figure 4. *Mtr4* knockout resulted in the incorrect nucleus-to-cytoplasm transport of transcripts without proper processing

(A) Statistics of retained intron number detected in total RNA-seq of different groups.

(B) Genomic distribution of total RNA-seq reads.

(C and D) Relative expression levels of introns quantified by FPKM in total RNA-seq. Introns whose levels changed by more than 2-fold are highlighted.

(E) Heatmap indicating relative expression levels of introns. Colored bars on the left of the heatmap represented the group division of intron expression patterns.

(F and G) IGV diagram showing abnormal intron retention after *Mtr4* deletion.

(H) FISH detection of the *Gdf9* introns (white arrows) in oocytes. Scale bars: 25 μm. n ≥ 12 per genotype.

(I) Diagram illustrating the design strategy of primers used in (J) and (K).

(J and K) RT-qPCR results confirming intron retention events in specific genes. n ≥ 3 per group.

(L) RT-qPCR results examining intron retention ratios in oocytes. n ≥ 3 per group.

Data are represented as mean ± SEM.
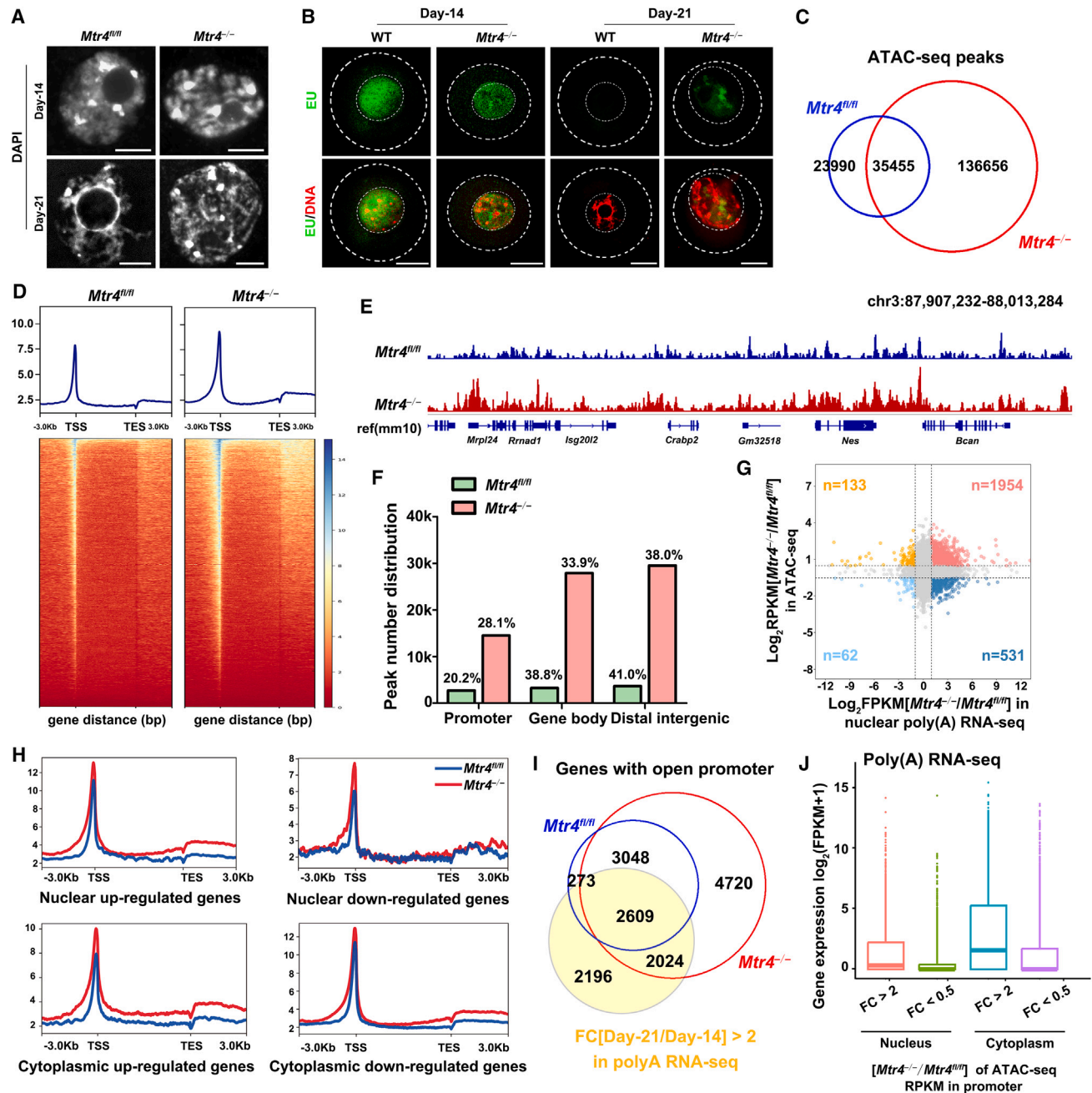
See also Figure S5 and Tables S2 and S3.

Figure 5. Chromatin structure and accessibility affected by *Mtr4* knockout in mouse oocytes

(A) DAPI staining showing the chromatin configurations in oocytes on days 14 and 21. $n \geq 24$ per group.

(B) EU fluorescent staining for the transcriptional activity of mRNA in oocytes. Scale bars: 25 μm. $n \geq 15$ per group.

(C) Venn diagram showing all ATAC-seq peaks detected in *Mtr4^fl/fl^* and *Mtr4*-null oocytes.

(D) Peak profile showing the relative density of the open chromatin area. Heatmap below indicates the peak distribution enrichment around the TSS.

(E) IGV snapshots of ATAC-seq peak distribution on chromatin.

(F) Whole-genome distribution of annotated peak using ATAC-seq in oocytes.

(G) Pairwise scatterplots showing fold changes of RNA-seq and ATAC-seq. Significantly changed genes are marked with colors and the corresponding numbers marked in the quadrants.

(H) Peak profile showing the relative density of the open chromatin area.

(I) Venn diagram showing genes annotated to obtain the open promoter in *Mtr4^fl/fl^* and *Mtr4*-null oocytes and genes accumulated during *Mtr4^fl/fl^* oocyte growth in poly(A) RNA-seq.

(J) Boxplot showing expression levels of genes in specific groups with upregulation or downregulation of chromatin accessibility level in the promoter region after *Mtr4* deletion.
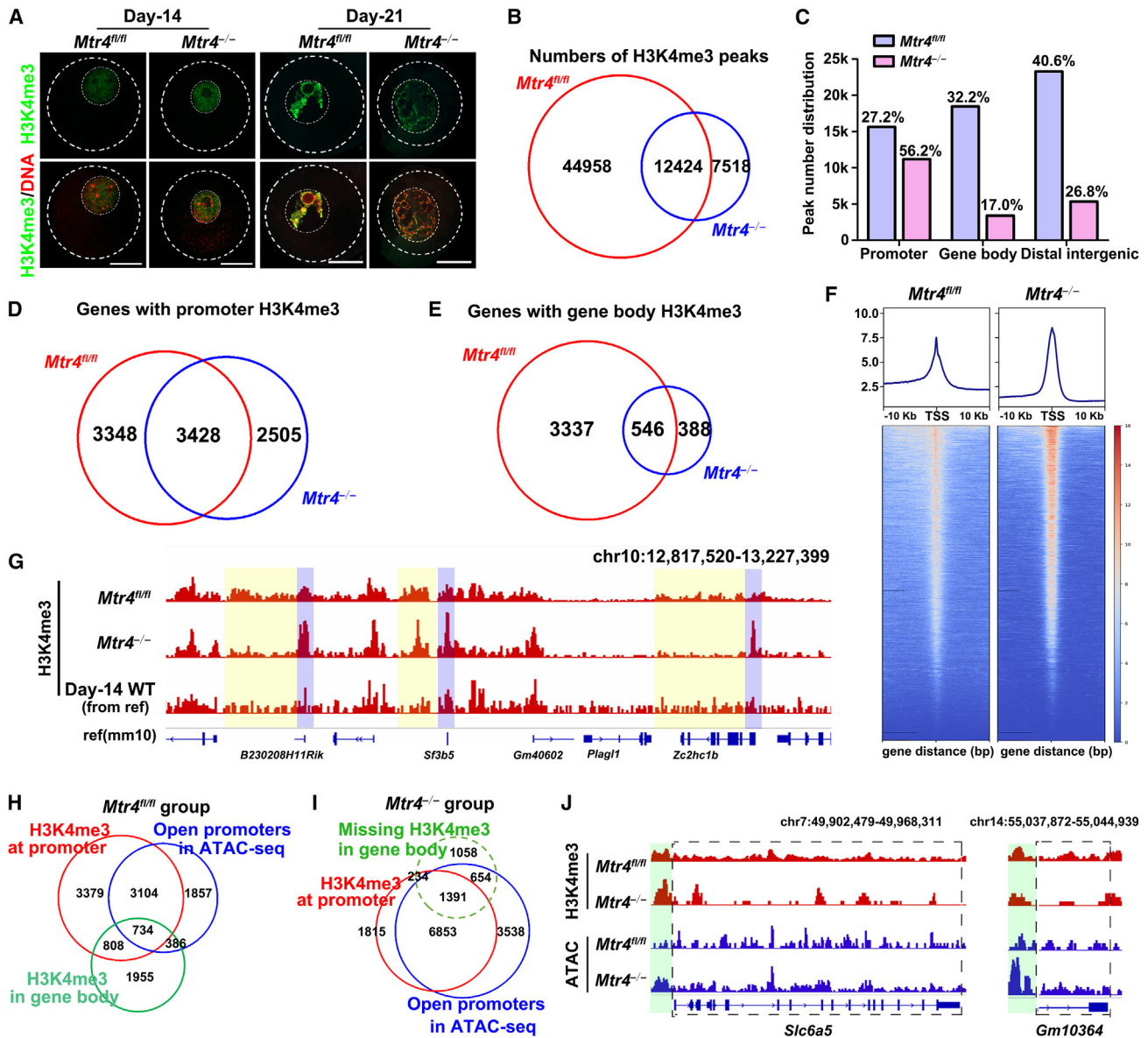
See also Figure S6.

Figure 6. MTR4 is required for the establishment of histone H3K4 trimethylation in mouse oocytes

(A) Immunofluorescence staining of H3K4me3 in oocytes. Scale bars: 25 μm.

(B) Venn diagram showing all H3K4me3 peaks detected using CUT&Tag in oocytes

(C) Genome-wide distribution of annotated peaks in oocytes.

(D and E) Venn diagram showing the number of genes with H3K4me3 peaks in the promoters (D) or gene bodies (E) in oocytes.

(F) Peak profile showing the relative density of H3K4me3 peaks around TSSs.

(G) IGV snapshots of H3K4me3 peaks' distribution in oocytes. Yellow background indicates the sharp peaks and the purple background indicates the broad peaks.

(H and I) Venn diagrams showing overlapping genes with open promoters and genes with H3K4me3 modifications at the promoter or gene body in the two groups.

(J) IGV snapshots of ATAC-seq peaks and H3K4me3 peaks. Green background indicates the promoter regions, whereas the gene body regions are framed by dashed lines.

See also Figure S6.

Subsequently, we compared the distribution of H3K4me3 signals and chromatin accessibility. Only 47.83% of the genes (3,838 out of 8,025 genes) with H3K4me3 modification at the promoter had an open promoter in $Mtr4^{fl/fl}$ oocytes (Figure 6H). Among the genes with H3K4me3 in the gene body, only 28.84% (1,120 of 3,883 genes) maintained open promoters, indicating that the distribution of non-canonical H3K4me3 in the gene body contributed to transcriptional silencing during oocyte maturation (Figure 6H). However, 81.96% (8,244 of 10,059) of the genes with H3K4me3 at the promoters were in the open
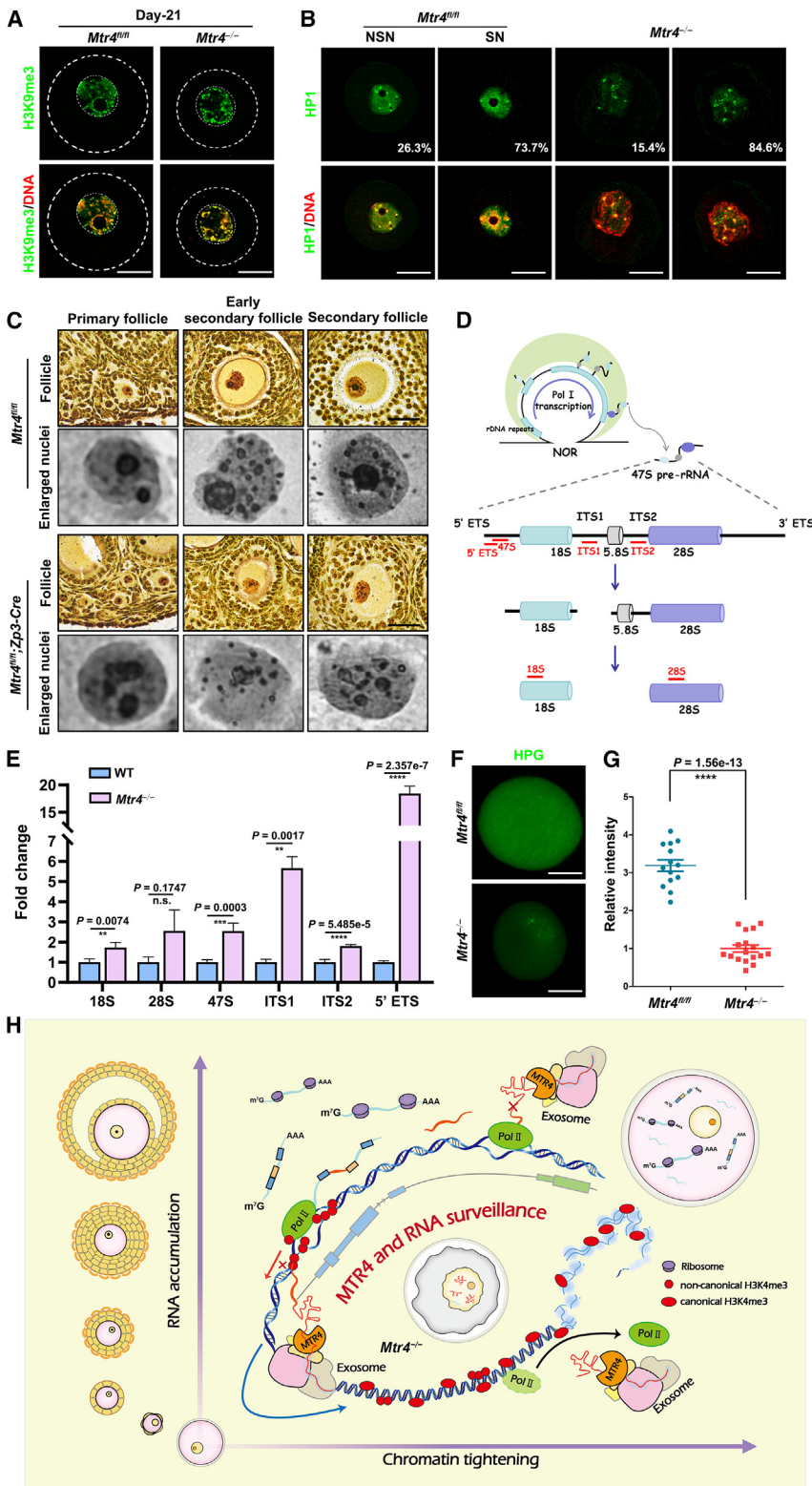
Figure 7. MTR4 is required for the formation of nucleolus-like structures in oocytes

(A and B) Immunofluorescence staining of H3K9me3 (A) and HP1 (B) in oocytes. $n \geq 14$ per genotype.

(C) Silver staining detecting active nucleolus organizer regions (black foci) and methyl green was co-stained. $n \geq 3$ per genotype.

(D) Diagram illustrating the processing steps of 47S pre-rRNA. Primers used in (E) were labeled in the diagram.

(E) Levels of rRNAs in day-21 oocytes detected by RT-qPCR. $n \geq 3$ per group.

(F and G) Translation activities detected by HPG (green) in oocytes.

(H) Roles of MTR4-mediated RNA surveillance in oocyte development.

Scale bars: 25 μm in (A), (B), (F), and (G); 20 μm in (C). Data are represented as mean ± SEM.

H3K4me3 modifications in the gene body after *Mtr4* deletion, 61.3% (2,045) had open promoters, suggesting that the failure of non-canonical H3K4me3 deposition in the gene body contributed to higher chromatin accessibility in *Mtr4*-null oocytes (Figure 6I). Pairwise scatterplots showed a significant positive correlation between an increase in chromatin accessibility and the establishment of H3K4me3 in promoters after *Mtr4* deletion (Figure S6E). Pairwise scatterplots generated from RNA-seq and CUT&Tag also showed a high correlation between H3K4me3 and the accumulation of nuclear transcripts, confirming the enrichment of H3K4me3 in promoters associated with transcription levels in *Mtr4*-null oocytes (Figure S6F). IGV snapshots provided typical examples that the deposition of H3K4me3 in promoter regions and the absence of H3K4me3 in the gene body likely affected chromatin accessibility in *Mtr4*-null oocytes (Figure 6J).

MTR4 is required for rRNA homeostasis and nucleolus-like structure formation during oocyte maturation

In addition to influencing chromatin accessibility, *Mtr4* knockout disrupted nucleolus-like structures in oocytes on day 21 (Figures 5A and 7A). Heterochromatin markers H3K9me3 and heterochromatin protein 1 (HP1) were localized in a ring structure surrounding the nucleolar precursor body in *Mtr4*^{fl/fl} oocytes; however, this structure was not formed in *Mtr4*-null oocytes (Figures 7A and 7B). The nucleolus organizer region (NOR) is responsible for nuclear formation,

chromatin state in *Mtr4*-null oocytes (Figure 6I), suggesting an increased association of H3K4me3 with the open promoter regions in *Mtr4*-null oocytes. Among the 3,337 genes that lost

Developmental Cell
Article

CellPress

and the acidic proteins in this region can be stained with AgNO₃. Dark foci in the nucleus indicated NOR activation (Figure 7C). In primordial and primary follicles, NOR activation did not differ between *Mtr4^fl/fl^* and *Mtr4*-null oocytes. Growing oocytes in secondary follicles of *Mtr4^fl/fl^* mice obtained the main large active NOR and many small NORs, whereas both NORs were much smaller in *Mtr4*-null oocytes at the same stage (Figure 7C).

According to the processing steps of the 47s pre-rRNA, we detected multiple forms of rRNAs (Figure 7D). RT-qPCR results showed that all types of rRNAs detected were upregulated in *Mtr4*-null oocytes, especially the 5′ external transcribed spacer (ETS), the splicing of which was reported to be associated with MTR4 in mice (Figure 7E).[43] The protein translation activity examined using the L-homopropargylglycine (HPG) incorporation assay was impaired due to the dysfunction of the nucleolus after *Mtr4* knockout (Figures 7F and 7G). Therefore, RNA surveillance-dependent chromatin changes are required for nucleolus-like structure formation and rRNA homeostasis during oocyte maturation.

DISCUSSION

This study provides evidence that the MTR4-mediated RNA surveillance mechanism participates in nascent RNA processing and fate decisions and ensures nuclear waste RNA clearance to maintain a healthy nuclear environment. Using nucleus-cytoplasm separation and sequencing, we discovered that, under normal conditions, the RNA content in the nucleus continues to decrease as oocytes mature. Disruption of RNA surveillance by *Mtr4* deletion leads to the accumulation of RNAs with unprocessed introns and incomplete transcript structures in the nucleus. Deleting genes encoding other exosome-associated factors, including *Exosc3*, *Exosc10*, and *Pabpn1*, leads to similar oogenesis defects and decreases developmental potential.[26,44,45] However, among all the exosome-component-null systems, *Mtr4*-null oocytes had the most severe chromatin defects, which may be related to the function of MTR4 in unwinding advanced RNA structures in the nucleus. The accumulation of unprocessed RNAs in the nucleus results in the loss of chromatin structure and failure of configuration transition, as demonstrated by the phenotypic profile and ATAC-seq in this study. Based on the analyses of oocyte-specific *Mtr4*-knockout mice, we propose three potential mechanisms by which RNA surveillance controls nuclear maturation in a feedback manner.

First, the loss of MTR4 and the accumulation of retained nuclear RNAs may interfere with nuclear compartmentalization. A previous study demonstrated that RNAs form high-concentration territories and bind to diffusible regulators to guide them into compartments to regulate essential nuclear functions, including RNA processing, heterochromatin assembly, and gene regulation.[37] Abnormal nuclear RNA condensation caused by MTR4 deletion leads to the dysfunction of nuclear compartment formation, and proper chromatin configuration changes essential for oocyte maturation are impaired as well.

Second, MTR4-mediated RNA surveillance is required to restrict the localization of RNA Pol II to genomic DNA and inhibit nonspecific genomic transcriptional activities, including nonsense transcription from intergenic regions and leakage transcription at gene promoters. A recent study suggested that the

accumulation of RNAs brought significant negative charges in the nucleus, which might weaken the interaction between hyperphosphorylated RNA Pol II and the chromatin template, both carrying substantial negative charges, implying the importance of RNA homeostasis for the nuclear environment.[46] The loss of MTR4 may cause persistent and perverse docking of RNA Pol II and its transcription products in the genome, thereby impairing chromatin condensation and heterochromatin formation, as demonstrated in Figure 5.

Third, persistent and perverse transcription and failure of nuclear compartmentation may prevent epigenetic maturation during oogenesis, particularly the establishment of non-canonical H3K4me3 peaks. It has been established that the sharp H3K4me3 peaks in gene promoters facilitate transcription, but the broad H3K4me3 peaks in gene bodies and distal intergenic regions are responsible for genome silencing in fully grown oocytes.[42,47–49] The results in Figure 6 agree with these observations and indicate a previously unknown role of RNA surveillance in regulating epigenetics during oogenesis.

Maintenance of an appropriate cell volume for different growth or stress conditions is a fundamental property of eukaryotes. Cells tend to maintain a roughly constant nucleus-to-cytoplasm volume ratio[50] to achieve a balance between transcription in the nucleus and translation in the cytoplasm.[51,52] When reaching the nucleus-cytoplasm volume ratio limit, cells choose cell fate as division or death. However, oocytes are a special system in which the nucleus-cytoplasm-volume ratio continued to decrease during the growth process. By comparing the nucleus-cytoplasm ratio, the oocyte size, and the corresponding mRNA enrichment between cytoplasm from *Mtr4^fl/fl^* and *Mtr4*-null oocytes, we suggest that proper mRNA accumulation in the cytoplasm, controlled by RNA surveillance, is a possible volume control factor during oocyte growth.

MTR4-mediated RNA surveillance may contribute to the expansion of oocyte volume in two ways. First, nascent RNAs are processed, degraded in the nucleus, or transported to the cytoplasm, all shown in this study to be under the control of MTR4-mediated RNA surveillance. Adequate mRNAs with advanced structures are transported and stored in the cytoplasm for subsequent protein translation. Key proteins for oocyte growth are translated, and other functional important proteins are stored as a foundation for meiotic maturation and early embryonic development. Under these circumstances, sufficient space should be provided to store massive amounts of mRNAs and protein at the fully grown GV stage. Second, the nucleolus is the main site for ribosome biogenesis, and assembly of the nucleolus is essential for subsequent protein translation. A healthy nuclear environment and rRNA processing provided by RNA surveillance are indispensable for ribosomal biogenesis. The dysfunction of RNA surveillance was shown in this study to affect the translational ability of oocytes. Thus, based on the previous theory that cell volume is controlled by the nucleus-cytoplasm ratio, we further propose that RNA surveillance in the nucleus contributes to cell volume expansion by providing adequate RNA accumulation and protein translation machines.

Limitations of the study
Poor oocyte developmental potential is one of the common reasons for female infertility. Here, we reported that MTR4-mediated

RNA surveillance mechanisms ensures oocyte growth and maturation. We reported in this study that MTR4-dependent RNA surveillance mechanisms directly participated in nuclear waste RNA clearance. Moreover, RNA surveillance has a previously unrecognized feedback function in maintaining a stable nuclear environment for chromatin configuration transition and is necessary to form a nucleolus-like structure in oocytes. However, how nuclear-retained waste transcripts interfere with chromatin configuration transition is still not entirely clear. We gave our hypothesis in the discussion section and more direct evidences ought to be explored in future research. Furthermore, observations in this study suggest that MTR4 ensures the establishment of non-canonical H3K4me3 on gene bodies, therefore building up a link between RNA surveillance and histone modification. To understand further links between RNA surveillance and chromatin status or histone modification, future studies regarding gene function, super-resolution microscopy imaging, and biological topology are needed to assess the role of retained transcripts in nuclei.

RESOURCE AVAILABILITY

Lead contact
Further information and requests for resources and reagents should be directed to and will be fulfilled by the lead contact, Heng-Yu Fan (hyfan@zju.edu.cn).

Materials availability
No unique reagents were generated in this study.

Data and code availability
Poly(A) RNA-seq data of whole oocytes have been deposited in the NCBI Gene Expression Omnibus database under the accession code GEO: GSE247848.

Poly(A) RNA-seq data of nuclei and cytoplasm from day-21 oocytes have been deposited in the NCBI Gene Expression Omnibus database under the accession code GEO: GSE247849.

Total RNA-seq data of nuclei and cytoplasm from day-21 oocyte have been deposited in the NCBI Gene Expression Omnibus database under the accession code GEO: GSE247850.

Total RNA-seq data of nuclei and cytoplasm from day-14 oocyte have been deposited in the NCBI Gene Expression Omnibus database under the accession code GEO: GSE262431.

ATAC-seq data have been deposited in the NCBI Gene Expression Omnibus database under the accession code GEO: GSE247846.

CUT&Tag data have been deposited in the NCBI Gene Expression Omnibus database under the accession code GEO: GSE247847.

This paper does not report original code.

Any additional information required to reanalyze the data reported in this paper is available from the lead contact upon request.

AUTHOR CONTRIBUTIONS

Conceptualization: H.-Y.F. and H.C.; methodology: Y.-W.W., G.-W.B., and H.-Y.F.; software: Y.-W.W.; investigation: Y.-W.W., Z.-Q.D., and Y.-K.W.; resources: H.-Y.F., Y.R., and H.C.; data curation: Y.-W.W.; writing – original draft: Y.-W.W.; writing – review & editing: H.-Y.F. and X.W.; visualization: Y.-W.W. and H.-Y.F.; supervision: H.-Y.F.; project administration: H.-Y.F.; funding acquisition: H.-Y.F.

DECLARATION OF INTERESTS

The authors declare no competing interests.

STAR★METHODS

Detailed methods are provided in the online version of this paper and include the following:

- KEY RESOURCES TABLE
- EXPERIMENTAL MODEL AND STUDY PARTICIPANT DETAILS
  - Mice
- METHOD DETAILS
  - Oocyte collection and *in vitro* culture
  - Immunofluorescence
  - EU incorporation assay
  - Western blot analysis
  - RNA isolation and qRT-PCR
  - Nucleus-cytoplasm separation experiment
  - Library construction of poly(A) RNA sequencing
  - Library construction of total RNA sequencing
  - Identification of intron retention events
  - ATAC-seq library construction
  - CUT&Tag library construction
  - Transcriptome analyses
  - ATAC-seq analyses
  - CUT&Tag analyses
  - Detection of transcription in oocytes
  - FISH
  - Histologic analysis and IHC
- QUANTIFICATION AND STATISTICAL ANALYSIS

SUPPLEMENTAL INFORMATION

Supplemental information can be found online at https://doi.org/10.1016/j.devcel.2024.09.009.

REFERENCES

1. Bukauskas, F.F., Kempf, C., and Weingart, R. (1992). Cytoplasmic Bridges and Gap-Junctions in an Insect Cell-Line (Aedes Albopictus). Exp. Physiol. *77*, 903–911. https://doi.org/10.1113/expphysiol.1992.sp003657.

2. Hamazaki, T.S., Nagahama, Y., Iuchi, I., and Yamagami, K. (1989). A Glycoprotein from the Liver Constitutes the Inner Layer of the Egg Envelope (Zona Pellucida Interna) of the Fish, Oryzias Latipes. Dev. Biol. *133*, 101–110. https://doi.org/10.1016/0012-1606(89)90301-1.

3. Spring, H., Meissneer, B., Fischer, R., Mouzaki, D., and Trendelenburg, M.F. (1996). Spatial arrangement of intra-nucleolar rDNA chromatin in amplified Xenopus oocyte nucleoli: Structural changes precede the onset of rDNA transcription. Int. J. Dev. Biol. *40*, 263–272.

4. Zhang, H., Risal, S., Gorre, N., Busayavalasa, K., Li, X., Shen, Y., Bosbach, B., Brännström, M., and Liu, K. (2014). Somatic Cells Initiate Primordial Follicle Activation and Govern the Development of Dormant Oocytes in Mice. Curr. Biol. *24*, 2501–2508. https://doi.org/10.1016/j.cub.2014.09.023.

5. Reddy, P., Liu, L., Adhikari, D., Jagarlamudi, K., Rajareddy, S., Shen, Y., Du, C., Tang, W.L., Hämäläinen, T., Peng, S.L., et al. (2008). Oocyte-specific deletion of. causes premature activation of the primordial follicle pool. Science *319*, 611–613. https://doi.org/10.1126/science.1152257.

Developmental Cell
Article

CellPress

6. Rong, Y., Ji, S.Y., Zhu, Y.Z., Wu, Y.W., Shen, L., and Fan, H.Y. (2019). ZAR1 and ZAR2 are required for oocyte meiotic maturation by regulating the maternal transcriptome and mRNA translational activation. Nucleic Acids Res. *47*, 11387–11402. https://doi.org/10.1093/nar/gkz863.

7. Cheng, S.Y., Altmeppen, G., So, C., Welp, L.M., Penir, S., Ruhwedel, T., Menelaou, K., Harasimov, K., Stützer, A., Blayney, M., et al. (2022). Mammalian oocytes store mRNAs in a mitochondria-associated membraneless compartment. Science *378*, eabq4835. https://doi.org/10.1126/science.abq4835.

8. Kurosaki, T., Popp, M.W., and Maquat, L.E. (2019). Quality and quantity control of gene expression by nonsense-mediated mRNA decay. Nat. Rev. Mol. Cell Biol. *20*, 406–420. https://doi.org/10.1038/s41580-019-0126-2.

9. Belair, C., Sim, S., and Wolin, S.L. (2018). Noncoding RNA Surveillance: The Ends Justify the Means. Chem. Rev. *118*, 4422–4447. https://doi.org/10.1021/acs.chemrev.7b00462.

10. Bresson, S., and Tollervey, D. (2018). Surveillance-ready transcription: nuclear RNA decay as a default fate. Open Biol. *8*, 170270. https://doi.org/10.1098/rsob.170270.

11. Sakaki, K., Yoshina, S., Shen, X.H., Han, J., DeSantis, M.R., Xiong, M., Mitani, S., and Kaufman, R.J. (2012). RNA surveillance is required for endoplasmic reticulum homeostasis. Proc. Natl. Acad. Sci. USA *109*, 8079–8084. https://doi.org/10.1073/pnas.1110589109.

12. Yang, F., Zhao, R., Fang, X.F., Huang, H.W., Xuan, Y., Ma, Y.T., Chen, H.Y., Cai, T., Qi, Y.J., and Xi, R.W. (2015). The RNA surveillance complex Pelo-Hbs1 is required for transposon silencing in the Drosophila germline. EMBO Rep. *16*, 965–974. https://doi.org/10.15252/embr.201540084.

13. Reimão-Pinto, M.M., Manzenreither, R.A., Burkard, T.R., Sledz, P., Jinek, M., Mechtler, K., and Ameres, S.L. (2016). Molecular basis for cytoplasmic RNA surveillance by uridylation-triggered decay in Drosophila. EMBO J. *35*, 2417–2434. https://doi.org/10.15252/embj.201695164.

14. Zinder, J.C., and Lima, C.D. (2017). Targeting RNA for processing or destruction by the eukaryotic RNA exosome and its cofactors. Genes Dev. *31*, 88–100. https://doi.org/10.1101/gad.294769.116.

15. Shoemaker, C.J., and Green, R. (2012). Translation drives mRNA quality control. Nat. Struct. Mol. Biol. *19*, 594–601. https://doi.org/10.1038/nsmb.2301.

16. Łabno, A., Tomecki, R., and Dziembowski, A. (2016). Cytoplasmic RNA decay pathways - Enzymes and mechanisms. Biochim. Biophys. Acta *1863*, 3125–3147. https://doi.org/10.1016/j.bbamcr.2016.09.023.

17. Mitchell, P., Petfalski, E., Shevchenko, A., Mann, M., and Tollervey, D. (1997). The exosome: A conserved eukaryotic RNA processing complex containing multiple 3′->5′ exoribonucleases. Cell *91*, 457–466. https://doi.org/10.1016/S0092-8674(00)80432-8.

18. Brouwer, R., Allmang, C., Raijmakers, R., van Aarssen, Y., Egberts, W.V., Petfalski, E., van Venrooij, W.J., Tollervey, D., and Pruijn, G.J.M. (2001). Three novel components of the human exosome. J. Biol. Chem. *276*, 6177–6184. https://doi.org/10.1074/jbc.M007603200.

19. Staals, R.H.J., Bronkhorst, A.W., Schilders, G., Slomovic, S., Schuster, G., Heck, A.J.R., Raijmakers, R., and Pruijn, G.J.M. (2010). Dis3-like 1: a novel exoribonuclease associated with the human exosome. EMBO J. *29*, 2358–2367. https://doi.org/10.1038/emboj.2010.122.

20. Taylor, L.L., Jackson, R.N., Rexhepaj, M., King, A.K., Lott, L.K., van Hoof, A., and Johnson, S.J. (2014). The Mtr4 ratchet helix and arch domain both function to promote RNA unwinding. Nucleic Acids Res. *42*, 13861–13872. https://doi.org/10.1093/nar/gku1208.

21. Lingaraju, M., Johnsen, D., Schlundt, A., Langer, L.M., Basquin, J., Sattler, M., Heick Jensen, T.H., Falk, S., and Conti, E. (2019). The MTR4 helicase recruits nuclear adaptors of the human RNA exosome using distinct arch-interacting motifs. Nat. Commun. *10*, 3393. https://doi.org/10.1038/s41467-019-11339-x.

22. Lange, H., Sement, F.M., and Gagliardi, D. (2017). MTR4, a putative RNA helicase and exosome co-factor, is required for proper rRNA biogenesis and development in Arabidopsis thaliana (vol 68, pg 51, 2011). Plant J. *91*, 355–356. https://doi.org/10.1111/tpj.13594.

23. Weick, E.M., Puno, M.R., Januszyk, K., Zinder, J.C., DiMattia, M.A., and Lima, C.D. (2018). Helicase-Dependent RNA Decay Illuminated by a Cryo-EM Structure of a Human Nuclear RNA Exosome-MTR4 Complex. Cell *173*, 1663–1677.e21. https://doi.org/10.1016/j.cell.2018.05.041.

24. Jia, H.J., Wang, X.Y., Anderson, J.T., and Jankowsky, E. (2012). RNA unwinding by the Trf4/Air2/Mtr4 polyadenylation (TRAMP) complex. Proc. Natl. Acad. Sci. USA *109*, 7292–7297. https://doi.org/10.1073/pnas.1201085109.

25. Meola, N., Domanski, M., Karadoulama, E., Chen, Y., Gentil, C., Pultz, D., Vitting-Seerup, K., Lykke-Andersen, S., Andersen, J.S., Sandelin, A., et al. (2016). Identification of a Nuclear Exosome Decay Pathway for Processed Transcripts. Mol. Cell *64*, 520–533. https://doi.org/10.1016/j.molcel.2016.09.025.

26. Dai, X.X., Pi, S.B., Zhao, L.W., Wu, Y.W., Shen, J.L., Zhang, S.Y., Sha, Q.Q., and Fan, H.Y. (2022). PABPN1 functions as a hub in the assembly of nuclear poly(A) domains that are essential for mouse oocyte development. Sci. Adv. *8*, eabn9016. https://doi.org/10.1126/sciadv.abn9016.

27. Demini, L., Kervarrec, C., Guillot, L., Com, E., Lavigne, R., Kernanec, P.Y., Primig, M., Pineau, C., Petit, F.G., and Jamin, S.P. (2023). Inactivation of Exosc10 in the oocyte impairs oocyte development and maturation, leading to a depletion of the ovarian reserve in mice. Int. J. Biol. Sci. *19*, 1080–1093. https://doi.org/10.7150/ijbs.72889.

28. Davidson, L., Francis, L., Cordiner, R.A., Eaton, J.D., Estell, C., Macias, S., Cáceres, J.F., and West, S. (2019). Rapid Depletion of DIS3, EXOSC10, or XRN2 Reveals the Immediate Impact of Exoribonucleolysis on Nuclear RNA Metabolism and Transcriptional Control. Cell Rep. *26*, 2779–2791.e5. https://doi.org/10.1016/j.celrep.2019.02.012.

29. Huber, M.D., and Gerace, L. (2007). The size-wise nucleus: nuclear volume control in eukaryotes. J. Cell Biol. *179*, 583–584. https://doi.org/10.1083/jcb.200710156.

30. Braunschweig, U., Barbosa-Morais, N.L., Pan, Q., Nachman, E.N., Alipanahi, B., Gonatopoulos-Pournatzis, T., Frey, B., Irimia, M., and Blencowe, B.J. (2014). Widespread intron retention in mammals functionally tunes transcriptomes. Genome Res. *24*, 1774–1786. https://doi.org/10.1101/gr.177790.114.

31. Rekosh, D., and Hammarskjold, M.L. (2018). Intron retention in viruses and cellular genes: Detention, border controls and passports. Wiley Interdiscip. Rev. RNA *9*, e1470. https://doi.org/10.1002/wrna.1470.

32. Middleton, R., Gao, D.D., Thomas, A., Singh, B., Au, A., Wong, J.J.L., Bomane, A., Cosson, B., Eyras, E., Rasko, J.E.J., et al. (2017). IRFinder: assessing the impact of intron retention on mammalian gene expression. Genome Biol. *18*, 51. https://doi.org/10.1186/s13059-017-1184-4.

33. Zhang, B.J., Zheng, H., Huang, B., Li, W.Z., Xiang, Y.L., Peng, X., Ming, J., Wu, X.T., Zhang, Y., Xu, Q.H., et al. (2016). Allelic reprogramming of the histone modification H3K4me3 in early mammalian development. Nature *537*, 553–557. https://doi.org/10.1038/nature19361.

34. Sha, Q.Q., Dai, X.X., Jiang, J.C., Yu, C., Jiang, Y., Liu, J., Ou, X.H., Zhang, S.Y., and Fan, H.Y. (2018). CFP1 coordinates histone H3 lysine-4 trimethylation and meiotic cell cycle progression in mouse oocytes. Nat. Commun. *9*, 3477. https://doi.org/10.1038/s41467-018-05930-x.

35. Yu, C., Fan, X., Sha, Q.Q., Wang, H.H., Li, B.T., Dai, X.X., Shen, L., Liu, J., Wang, L., Liu, K., et al. (2017). CFP1 Regulates Histone H3K4 Trimethylation and Developmental Potential in Mouse Oocytes. Cell Rep. *20*, 1161–1172. https://doi.org/10.1016/j.celrep.2017.07.011.

36. Smith, K.P., Hall, L.L., and Lawrence, J.B. (2020). Nuclear hubs built on RNAs and clustered organization of the genome. Curr. Opin. Cell Biol. *64*, 67–76. https://doi.org/10.1016/j.ceb.2020.02.015.

37. Quinodoz, S.A., Jachowicz, J.W., Bhat, P., Ollikainen, N., Banerjee, A.K., Goronzy, I.N., Blanco, M.R., Chovanec, P., Chow, A., Markaki, Y., et al. (2021). RNA promotes the formation of spatial compartments in the nucleus. Cell *184*, 5775–5790.e30. https://doi.org/10.1016/j.cell.2021.10.014.

38. Palihati, M., and Saitoh, N. (2024). RNA in chromatin organization and nuclear architecture. Curr. Opin. Genet. Dev. 86, 102176. https://doi.org/10.1016/j.gde.2024.102176.

39. Misteli, T. (2005). Concepts in nuclear architecture. Bioessays 27, 477–487. https://doi.org/10.1002/bies.20226.

40. Zannino, L., Casali, C., Siciliani, S., and Biggiogera, M. (2021). The dynamics of the nuclear environment and their impact on gene function. J. Biochem. 169, 259–264. https://doi.org/10.1093/jb/mvaa091.

41. Sha, Q.Q., Jiang, Y., Yu, C., Xiang, Y.L., Dai, X.X., Jiang, J.C., Ou, X.H., and Fan, H.Y. (2020). CFP1-dependent histone H3K4 trimethylation in murine oocytes facilitates ovarian follicle recruitment and ovulation in a cell-nonautonomous manner. Cell. Mol. Life Sci. 77, 2997–3012. https://doi.org/10.1007/s00018-019-03322-y.

42. Andreu-Vieyra, C.V., Chen, R.H., Agno, J.E., Glaser, S., Anastassiadis, K., Stewart, A.F., and Matzuk, M.M. (2010). MLL2 Is Required in Oocytes for Bulk Histone 3 Lysine 4 Trimethylation and Transcriptional Silencing. PLoS Biol. 8, e1000453. https://doi.org/10.1371/journal.pbio.1000453.

43. Thoms, M., Thomson, E., Baßler, J., Gnädig, M., Griesel, S., and Hurt, E. (2015). The Exosome Is Recruited to RNA Substrates through Specific Adaptor Proteins. Cell 162, 1029–1038. https://doi.org/10.1016/j.cell.2015.07.060.

44. Chiu, A.C., Suzuki, H.I., Wu, X.B., Mahat, D.B., Kriz, A.J., and Sharp, P.A. (2018). Transcriptional Pause Sites Delineate Stable Nucleosome-Associated Premature Polyadenylation Suppressed by U1 snRNP. Mol. Cell 69, 648–663.e7. https://doi.org/10.1016/j.molcel.2018.01.006.

45. Marin-Vicente, C., Domingo-Prim, J., Eberle, A.B., and Visa, N. (2015). RRP6/EXOSC10 is required for the repair of DNA double-strand breaks by homologous recombination. J. Cell Sci. 128, 1097–1107. https://doi.org/10.1242/jcs.158733.

46. Han, X., Xing, L., Hong, Y., Zhang, X., Hao, B., Lu, J.Y., Huang, M., Wang, Z., Ma, S., Zhan, G., et al. (2024). Nuclear RNA homeostasis promotes systems-level coordination of cell fate and senescence. Cell Stem Cell 31, 694–716.e11. https://doi.org/10.1016/j.stem.2024.03.015.

47. Dahl, J.A., Jung, I., Aanes, H., Greggains, G.D., Manaf, A., Lerdrup, M., Li, G.Q., Kuan, S., Li, B., Lee, A.Y., et al. (2016). Broad histone H3K4me3 domains in mouse oocytes modulate maternal-to-zygotic transition. Nature 537, 548–552. https://doi.org/10.1038/nature19360.

48. Savić, N., Bär, D., Leone, S., Frommel, S.C., Weber, F.A., Vollenweider, E., Ferrari, E., Ziegler, U., Kaech, A., Shakhova, O., et al. (2014). lncRNA Maturation to Initiate Heterochromatin Formation in the Nucleolus Is Required for Exit from Pluripotency in ESCs. Cell Stem Cell 15, 720–734. https://doi.org/10.1016/j.stem.2014.10.005.

49. Wu, J., Xu, J., Liu, B., Yao, G., Wang, P., Lin, Z., Huang, B., Wang, X., Li, T., Shi, S., et al. (2018). Chromatin analysis in human early development reveals epigenetic transition during ZGA. Nature 557, 256–260. https://doi.org/10.1038/s41586-018-0080-8.

50. Cavalier-Smith, T. (2005). Economy, speed and size matter: Evolutionary forces driving nuclear genome miniaturization and expansion. Ann. Bot. 95, 147–175. https://doi.org/10.1093/aob/mci010.

51. Jorgensen, P., Edgington, N.P., Schneider, B.L., Rupes, I., Tyers, M., and Futcher, B. (2007). The size of the nucleus increases as yeast cells grow. Mol. Biol. Cell 18, 3523–3532. https://doi.org/10.1091/mbc.E06-10-0973.

52. Cantwell, H., and Nurse, P. (2019). Unravelling nuclear size control. Curr. Genet. 65, 1281–1285. https://doi.org/10.1007/s00294-019-00999-3.

53. Kim, D., and Salzberg, S.L. (2011). TopHat-Fusion: an algorithm for discovery of novel fusion transcripts. Genome Biol. 12, R72. https://doi.org/10.1186/gb-2011-12-8-r72.

54. Robinson, J.T., Thorvaldsdóttir, H., Winckler, W., Guttman, M., Lander, E.S., Getz, G., and Mesirov, J.P. (2011). Integrative genomics viewer. Nat. Biotechnol. 29, 24–26. https://doi.org/10.1038/nbt.1754.

55. Schneider, C.A., Rasband, W.S., and Eliceiri, K.W. (2012). NIH Image to ImageJ: 25 years of image analysis. Nat. Methods 9, 671–675. https://doi.org/10.1038/nmeth.2089.

56. Langmead, B., and Salzberg, S.L. (2012). Fast gapped-read alignment with Bowtie 2. Nat. Methods 9, 357–359. https://doi.org/10.1038/nmeth.1923.

57. Ramírez, F., Ryan, D.P., Grüning, B., Bhardwaj, V., Kilpert, F., Richter, A.S., Heyne, S., Dündar, F., and Manke, T. (2016). deepTools2: a next generation web server for deep-sequencing data analysis. Nucleic Acids Res. 44, W160–W165. https://doi.org/10.1093/nar/gkw257.

58. Picelli, S., Faridani, O.R., Björklund, A.K., Winberg, G., Sagasser, S., and Sandberg, R. (2014). Full-length RNA-seq from single cells using Smart-seq2. Nat. Protoc. 9, 171–181. https://doi.org/10.1038/nprot.2014.006.

Developmental Cell
Article

CellPress

STAR★METHODS

KEY RESOURCES TABLE

REAGENT or RESOURCE	SOURCE	IDENTIFIER
Antibodies		
MTR4	Abcam	Cat# ab70551
SKIV2L2	BETHYL	Cat IHC-00470
PABPN1	Bethy	Cat A303-523A
SRSF2	Sigma	Cat# SAB4200725
pS2	Abcam	Cat# ab5095
H3K4me3	Cell Signaling Technology	Cat# C42D8
H3K9me3	Abcam	Cat# ab8898
HP1	Abcam	Cat# ab109028
Chemicals, peptides, and recombinant proteins		
TRIzol Reagent	ThermoFisher Scientific	Cat# 15596026
M2 medium	Sigma	Cat# M7167
M16 medium	Sigma	Cat# M7292
PFA	Sigma	Cat 158127
Critical commercial assays		
ERCC spike-in control mix	Invitrogen	Cat# 4456740
TruePrep DNA Library Prep Kit V2 from Illumina	Vazyme	Cat# TD503
Abclonal rRNA Depletion module	Abclonal	Cat# RK20348
Abclonal Fast RNA-seq Lib Prep Kit V2	Abclonal	Cat# RK20306
Chromatin Profile Kit for Illumina	Novoprotein	Cat# N248
NovoNGS CUT&Tag 3.0 High sensitivity Kit	Novoprotein	Cat# N259
AgNOR	LMAI-Bio	Cat# LM-44361-1
Click-iT Plus OPP Protein Synthesis Assay Kits	Invitrogen	Cat# C10456
Click-iT RNA Alexa Fluor488 Imaging Kits	Invitrogen	Cat# C10329
mMESSAGE mMACHINE T7 Kit	Ambion	Cat# AM1344
mMESSAGE mMACHINE SP6 Kit	Ambion	Cat# AM1340
Poly(A) tailing Kit	AM1350	Cat# AM1350
Deposited data		
Raw and analyzed poly(A) RNA-seq data of whole oocytes	This paper	GEO: GSE247848
Raw and analyzed poly(A) RNA-seq data of nuclei and cytoplasm from Day-21 oocytes	This paper	GEO: GSE247849
Raw and analyzed total RNA-seq data of nuclei and cytoplasm from Day-21 oocytes	This paper	GEO: GSE247850
Raw and analyzed total RNA-seq data of nuclei and cytoplasm from Day-14 oocytes	This paper	GEO: GSE262431
Raw and analyzed data of ATAC-seq	This paper	GEO: GSE247846
Raw and analyzed data of CUT&Tag	This paper	GEO: GSE247847
Experimental models: Organisms/strains		
Mouse: C57/BL *Mtr4^{fl/fl}*	Gift from Hong Cheng(Chinese Academy of Sciences)	N/A
Mouse: C57/BL *Mtr4^{fl/fl};Zp3-cre*	This paper	N/A
Oligonucleotides		
See Table S5 for primer sequences	This paper	N/A

(Continued on next page)

Continued

REAGENT or RESOURCE	SOURCE	IDENTIFIER
Recombinant DNA		
Plasmid: *Gfp-Dcaf13*	This paper	N/A
Plasmid: *Gfp-Mtr4*	This paper	N/A
Plasmid: *mCherry-Mtr4*	This paper	N/A
Software and algorithms		
IRFinder	Middleton et al.[32]	https://github.com/williamritchie/IRFinder/
tophat	Kim and Salzberg[53]	https://ccb.jhu.edu/software/tophat/index.shtml
IGV	Robinson et al.[54]	https://www.igv.org/
GraphPad Prism	GraphPad Software	https://www.graphpad.com
ImageJ	Schneider et al.[55]	https://imagej.net/
Bowtie2	Langmead and Salzberg[56]	http://bowtie-bio.sourceforge.net/bowtie2/index.shtml
Deeptools	Ramírez et al.[57]	https://deeptools.readthedocs.io/en/latest/
Other		
Information of sequencing data see Tables S1, S2, and S3	This paper	N/A

EXPERIMENTAL MODEL AND STUDY PARTICIPANT DETAILS

Mice
All the mouse strains had a C57B6 background. *Mtr4^{fl/fl};Zp3-Cre* mice were established by crossing *Mtr4* flox allele mice with *Zp3-Cre* transgenic mice. Mice were bred under specific-pathogen-free conditions in a controlled environment of 20–22°C, with a 12/12 h light/dark cycle, 50–70% humidity, and food and water provided *ad libitum*.

METHOD DETAILS

Oocyte collection and *in vitro* culture
Growing and fully grown oocytes were collected from 14- and 21-day-old mice, respectively. Oocytes at the GV stage were harvested in M2 medium (M7167; Sigma-Aldrich) and cultured in mini-drops of M16 medium (M7292; Sigma-Aldrich) covered with mineral oil (M5310; Sigma-Aldrich) at 37°C in a 5% CO_2 atmosphere.

Immunofluorescence
The oocytes were fixed in 4% paraformaldehyde in phosphate-buffered saline (PBS) for 30 min at room temperature and permeabilized for 15–30 min in PBS containing 0.1% Triton X-100. After blocking with 1% bovine serum albumin in PBS containing 0.1% Tween 20 (PBST), oocytes were incubated with primary antibodies diluted in blocking solution at 25°C for 1 h and then incubated with Alexa Fluor 594-conjugated or 488-conjugated secondary antibodies (Molecular Probes). The slides were mounted using VectaShield with DAPI (Vector Laboratories). Imaging of the oocytes after immunofluorescence was performed using a Zeiss LSM710 confocal microscope. The antibodies used are listed in Table S4.

EU incorporation assay
Oocytes were cultured in M16 medium containing 1 mM EU for 1 h. Fixation, permeabilization, and staining were performed using the Click-iT RNA Alexa Fluor 488 Imaging Kit (Life Technologies) according to the manufacturer's protocol. The embryos were imaged using a Zeiss LSM710 confocal microscope.

Western blot analysis
Oocytes were lysed in β-mercaptoethanol containing loading buffer and heated at 95°C for 5 min. Total oocyte proteins were separated using sodium dodecyl sulfate-polyacrylamide gel electrophoresis and electrophoretically transferred onto polyvinylidene fluoride membranes (Millipore). Membranes were blocked in Tris-buffered saline with 0.1% Tween 20 (TBST) containing 5% defatted milk for 30 min. After being probed with primary antibodies at 4°C overnight, the membranes were washed in TBST, incubated with a horseradish peroxidase-linked secondary antibody for 1 h and washed three times in TBST. The primary antibodies used are listed in Table S4.

Developmental Cell
Article

🔗 **CellPress**

RNA isolation and qRT-PCR

Oocytes were collected and lysed directly with 0.2% Triton X-100 and 4 IU RNase inhibitor. The standard reverse transcription protocol was followed using random primers and primer transcript II reverse transcriptase (Takara Bio). Real-time PCR was performed using Power SYBR Green PCR Master Mix (Applied Biosystems, Life Technologies) and an Applied Biosystems 7500 Real-Time PCR system. Relative mRNA levels were calculated and compared with the respective cycle threshold (ct) values normalized to endogenous *Gapdh* mRNA levels. Specifically, the gene expression levels were calculated by 2ΔCt (2ΔCt(gene-*Gapdh*)). The relative transcript levels of the samples were compared with those of the controls, and fold changes were determined. Each experiment was performed in triplicates. The primer sequences are listed in Table S5.

Nucleus-cytoplasm separation experiment

Oocytes were cultured with 1 μg/mL Cytochalasin B for 30 min, together with 2 μM milrinone to prevent GV breakdown. The nuclei and cytoplasms were separated using a micromanipulation needle tip. After washing three times in 0.2% bovine serum albumin, samples were collected in the DNase/RNase-free tubes and stored at −80°C for further library construction.

Library construction of poly(A) RNA sequencing

Samples from different stages were collected from WT, *Mtr4*$^{fl/f}$, and *Mtr4*$^{fl/fl}$;*Zp3-Cre* mice, with 10 oocytes per sample. Each sample was directly lysed with 2 μL of lysis buffer (0.2% Triton X-100 and RNase inhibitor) and 0.2 μL of 1:1000 diluted ERCC. The RNA in the cell lysis buffer was reverse-transcribed according to the Smart-seq2 method.[58] Qsep analysis of cDNA quality was conducted to confirm that the main peaks of the cDNA library pool were more than 1000 bp. The full-length cDNA library was fragmented using the TruePrep DNA Library Prep Kit V2 from Illumina (Vazyme, TD503). DNA fragments were selected, and the final sequencing libraries were constructed from 300–400 bp of the amplified cDNA. Sequencing data were extracted on the Illumina HiSeq X Ten platform in the 150 bp paired-end mode.

Library construction of total RNA sequencing

Samples from different stages were collected from WT, *Mtr4*$^{fl/fl}$, and *Mtr4*$^{fl/fl}$;*Zp3-Cre* mice, with 10 oocytes per sample. Total RNA was extracted using the TRIzol reagent. After removing rRNAs using the Abclonal rRNA Depletion module, total RNA was used as input for library construction using the Abclonal Fast RNA-seq Lib Prep Kit V2. DNA fragments were selected, and the final sequencing libraries were constructed from 300–400 bp of the amplified cDNAs. Sequencing data were extracted on the Illumina HiSeq X Ten platform in the 150 bp paired-end mode.

Identification of intron retention events

IRFinder software was used to calculate intron retention ratio.[32] The IR ratio quantifies the portion of a given intron not removed by splicing mechanisms, ranging from 0 to 1. To b specific, the IR ratio is calculated as intronic abundance divided by the sum of intronic abundance and normal splicing abundance ($IR - ratio = \frac{Intronic\ abundance}{Intronic\ abundance + exonic\ abundance}$), as illustrated by IRFinder software. Our standard included an IR-ratio > 0.3 and a low-covering group deletion. Distributions of introns were calculated as the distance between the intron start site and the gene start site divided by the length of the gene.

ATAC-seq library construction

Samples were extracted from Day-21 ovaries of *Mtr4*$^{fl/fl}$ and *Mtr4*$^{fl/fl}$;*Zp3-Cre* mice, with 50 oocytes per sample. The oocytes were lysed in a buffer containing 0.05% digitonin, 0.5% NP-40, and 0.5% Tween20. Tn5 enzyme in Chromatin Profile Kit for Illumina (Novoprotein; N248) was used to fragment chromatin at 37°C for 30 min and immediately stopped adding the stop buffer. After purifying DNA using DNA clean beads, PCR was performed to amplify the library for 15 cycles using the following PCR conditions: 72°C for 3 min; 98°C for 30 s; and thermocycling at 98°C for 15 s, 60°C for 15 s, and 72°C for 8 s; following by 72°C for 2 min. After the PCR reactions, the libraries were purified with the 1.2X DNA cleaning beads.

CUT&Tag library construction

Samples were extracted from Day-21 ovaries of *Mtr4*$^{fl/fl}$ and *Mtr4*$^{fl/fl}$;*Zp3-Cre* mice, with 120 oocytes per sample. A NovoNGS CUT&Tag 3.0 High sensitivity Kit (Novoprotein; N259; Illumina) was used for library construction. The protocol used in this study followed the manufacturer's instructions with several modifications, including antibody concentrations of 1:100 for the primary antibody (CST: 9751) and 1:200 for the secondary antibody and 16 PCR cycles for amplification.

Transcriptome analyses

RNA sequencing was performed using biological replicates of each sample. Raw data were trimmed into 50-bp reads and mapped to the mouse reference genome (mm9) using TopHat (v2.1.1) with default parameters.[53] Uniquely mapped reads were assembled into transcripts using reference annotations (University of California at Santa Cruz Gene Models) and Cufflinks (v2.2.1). Relative gene expression levels were quantified using FPKM, and the final FPKM values were averaged and corrected using the ERCC spike-in. Genes with a multiple of fold change > 2 and p-vlaue < 0.05 were considered as differentially expressed genes.

 CellPress

Developmental Cell
Article

Gene transfer format (gtf) documents including only first exons or last exons were generated separately using standard gtf document according to the exon sorting number. Expression levels of first or last exons were quantified from the separated gtf documents with uniquely mapped reads.

Statistical analyses and figure drawings were performed using the R software (http://www.rproject.org). The Spearman correlation coefficient (rs) was calculated using the "cor" function, and the complete linkage hierarchical algorithm was used to cluster the genes. Scatter plots were performed using ggplot2, dplyr, ggrepel and cowplot packages in R software. Boxplots were performed using ggplot2 and ggpubr packages in R software.

ATAC-seq analyses

The pair-end ATAC-seq reads were aligned to the mm10 reference genome using Bowtie2 software. All unmapped, non-uniquely mapped, PCR-duplicated, and mitochondrial reads were removed before subsequent analyses. Read counts were normalized using the reads per kilobase per million mapped reads method with bamCoverage instruction, and the Macs2 software was used to identify the narrow peaks in the downstream analysis. ATAC-seq peak profiles were generated from computeMatrix instruction using the -referencePoint TSS arguments.

CUT&Tag analyses

Pair-end CUT&Tag reads were trimmed with trim_galore and aligned to the mm10 reference using the Bowtie2 software[56] using the following arguments: bowtie2 –end-to-end –very-sensitive –no-mixed –phred33 -I 10 -X 1000 -p 8 -x reference -1 sample_R1.fq.gz -2 sample_R2.fq.gz -S sample.raw.sam. All unmapped, non-uniquely mapped, PCR-duplicated, and mitochondrial reads were removed before subsequent analyses. Read counts were normalized using the reads per kilobase per million mapped reads method with bamCoverage instruction, and the Macs2 software was used to call the peaks in the downstream analyses. CUT&Tag peak profiles were generated from computeMatrix instruction using the -referencePoint TSS arguments.[57]

Detection of transcription in oocytes

The transcriptional ability of oocytes was detected by culturing them in M16 medium containing 1 mM EU for 1 h. EU staining was performed using a Click-iT RNA Alexa Fluor 488 Imaging Kit (Life Technologies), according to the manufacturer's instructions. Oocytes were imaged using a Zeiss LSM710 confocal microscope, and relative signal intensities were quantified using ImageJ software.

FISH

Oocytes were collected from Day-14 or Day-21 mice and fixed with 4% paraformaldehyde in RNase-free PBS for 15 min. Fixed oocytes were permeabilized in PBS containing 2% Triton X-100 and an RNase inhibitor for 15 min. After being blocked with WR Buffer for 15 min, the oocytes were incubated with an RNA probe (0.2 μM in hybridization buffer) for 4–20 h at 37°C. After washing thrice in WR Buffer (15 min each time), the oocytes were labeled with DAPI for 5 min. The oocytes were imaged using a Zeiss LSM710 confocal microscope.

Histologic analysis and IHC

Ovary samples were collected and fixed overnight in 4% formalin. After standard dehydration procedures, samples were embedded in paraffin, sectioned with 5-μm thickness, deparaffinized and rehydrated, and stained with hematoxylin and eosin. For IHC staining, sections were incubated in primary antibody overnight at 4°C, washed three times with PBS, and then incubated in biotin-labeled secondary antibodies for 30 min at 25°C. The staining procedure followed the instructions of the Vectastain ABC kit and 3,3′- diaminobenzidine peroxidase substrate kit (Vector Laboratories, Burlingame, California). Ovarian sections were counterstained with hematoxylin after IHC staining.

QUANTIFICATION AND STATISTICAL ANALYSIS

Each experiment was repeated at least thrice. Results are given as mean ± SEM. The results of the two experimental groups were compared using two-tailed unpaired Student's t-tests. Statistically significant values of $P < 0.05$, $P < 0.01$, and $P < 0.001$ are indicated by asterisks (*), (**), and (***), respectively. Independent two-group Wilcoxon rank-sum tests were used to compare the distributions using the Wilcoxon test function in R. Pearson's R coefficient was calculated using the cor function with default parameters, and the complete method was used to cluster the genes.